

Latent Neural PDE Solver: a reduced-order modelling framework for partial differential equations

Zijie Li,^{†,‡} Saurabh Patil,^{†,‡} Francis Ogoke,^{†,‡} Dule Shu,[†] Wilson Zhen,[†]
Michael Schneier,[¶] John R. Buchanan, Jr.,[¶] and Amir Barati Farimani^{*,†}

[†]*Department of Mechanical Engineering, Carnegie Mellon University, Pittsburgh PA, USA*

[‡]*Contributed equally to this work*

[¶]*Naval Nuclear Laboratory, West Mifflin PA, USA*

E-mail: barati@cmu.edu

Abstract

Neural networks have shown promising potential in accelerating the numerical simulation of systems governed by partial differential equations (PDEs). Different from many existing neural network surrogates operating on high-dimensional discretized fields, we propose to learn the dynamics of the system in the latent space with much coarser discretizations. In our proposed framework - Latent Neural PDE Solver (LNS), a non-linear autoencoder is first trained to project the full-order representation of the system onto the mesh-reduced space, then a temporal model is trained to predict the future state in this mesh-reduced space. This reduction process simplifies the training of the temporal model by greatly reducing the computational cost accompanying a fine discretization and enables more efficient backprop-through-time training. We study the capability of the proposed framework and several other popular neural PDE solvers on various types of systems including single-phase and multi-phase flows along with

varying system parameters. We showcase that it has competitive accuracy and efficiency compared to the neural PDE solver that operates on full-order space.

1 Introduction

Many intricate physical processes, from the interaction of protein dynamics to the movement of a celestial body, can be described by time-dependent partial differential equations (PDEs). The simulation of these processes is often conducted by solving these equations numerically, which requires fine discretization to resolve the necessary spatiotemporal domain to reach convergence. Deep neural network surrogates¹⁻⁶ recently emerged as a computationally less-expensive alternative, with the potential to improve the efficiency of simulation by relaxing the requirement for fine discretization and attaining a higher accuracy on coarser grids compared to classical numerical solver^{2,6,7}.

For time-dependent systems, many neural-network-based models address the problem by approximating the solution operator \mathcal{G} that maps the state u_t to $u_{t+\Delta t}$, where the input and output are sampled on discretization grid $\{D_i, D_h\}$ respectively. The input discretization grid can either remain unchanged between every layer inside the network^{2,6,8}, or fit into a hierarchical structure⁹⁻¹⁴ that resembles the V-Cycle in classical multi-grid methods. Hierarchical structures have also been a common model architectural choice in the field of image segmentation¹⁵ and generation¹⁶ given their capability for utilizing multi-scale information.

In contrast to the aforementioned approaches, especially those that utilize a hierarchical grid structure, our work studies the effect of decoupling dynamics prediction from upsampling/downsampling processes. Specifically, the neural network for predicting the forward dynamics (which we defined as a propagator) only operates on the coarsest resolution, while a deep autoencoder is pre-trained to compress the data from the original discretization grid D_i to the coarse grid D_l (e.g. from a 64×64 grid to an 8×8 grid). As the propagator

network operates on a lower dimensional space, the training cost is greatly reduced and can be potentially adapted to unrolled training with a longer backprop-through-time (BPTT) horizon, which is often observed to be helpful to long-term stability^{17–19}. We parameterize the model with a convolutional neural network along with several other components that are popular in neural PDE solvers, including several variants of attention. We test the proposed framework on different time-dependent PDEs with different flow types and boundary conditions. We showcase that the model can achieve efficient data compression and accurate prediction of complicated forward dynamics with significantly reduction in the computational cost associated with backpropagation through time. The proposed framework highlights an alternative for choosing the space for neural PDE solver to operate on.

2 Related works

Neural PDE solver Neural PDE solvers can be categorized into the following groups based on their model design. The first group employs neural networks with mesh-specific architectures, such as convolutional layers for uniform meshes or graph layers for irregular meshes. These networks learn spatiotemporal correlations within PDE data without the knowledge of the underlying equations^{4–7,9,11,13,14,20–25}. Such a data-driven approach is useful for systems with unknown or partially known physics, such as large-scale climate modeling^{26–29}. The second group, known as Physics-Informed Neural Networks (PINNs)^{1,30–34}, treats neural networks as a parameterization of the solution function. PINNs incorporate knowledge of governing equations into the loss function, including PDE residuals and consistency with boundary and initial conditions. Unlike the first group, PINNs can be trained solely on equation loss and do not necessarily require input-target data pairs. The third group, known as the neural operators^{2,3,8,10,35–46}, is designed to learn the mapping between function spaces. For a certain family of PDEs, neural operators have the potential to generalize and adapt to multiple discretizations. DeepONet³ presents a pragmatic implementation of the universal

operator approximation theorem⁴⁷. Meanwhile, the concurrent research⁴⁸ in the form of the graph neural operator proposes a trainable kernel integral for approximating solution operators in parametric PDEs. Their follow-up work, Fourier Neural Operator (FNO)², has demonstrated high accuracy and efficiency in solving specific types of problems. Different function bases such as Fourier^{2,49–51} / wavelet bases⁴¹, the learned feature map from attention layers^{8,42}, or Green’s function approximation^{52,53}, have been used for operator learning. For more physically consistent predictions, neural operator training can be combined with PINN principles^{54–57}.

Two-stage model for image compression and synthesis The utilization of a two-stage model for image synthesis has gained significant attention in the field of computer vision in recent years. Vector Quantized Variational Autoencoders (VQ-VAEs)⁵⁸ adopt a two-stage approach for generating images within a latent space. In the initial stage, the approach compresses images into this latent space, using model components such as an encoder, a codebook, and a decoder. Subsequently, in the second stage, a latent model is introduced to predict the latent characteristics of the compressed images, and the decoder from the first stage is used to transform the predicted latent representation back into image pixels. Vector Quantized Generative Adversarial Networks (VQ-GANs)⁵⁹ are developed to scale autoregressive transformers to large image generation by employing adversarial and perceptual objectives for first-stage training. Most recently, several works have developed latent diffusion models with promising results ranging from image⁶⁰ to point clouds⁶¹.

Latent space modelling for time-dependent PDE problems Many of the existing time-dependent neural PDE solvers have employed Encoder-Process-Decoder (EPD) scheme, used to map the input solution at time t to the subsequent time step^{4–6,62–64}. In these models, the input mesh and output mesh are usually the same, where the encoder and decoder are pointwise operator that does not affect the underlying discretization. As an alternative, researchers have explored propagating the system dynamics in the latent space with coarsened

mesh, aiming to reduce computational complexity and minimize memory usage^{65–70}. Evolving the system dynamics in latent space can involve utilization of recurrent neural networks like Long Short-Term Memory⁶⁷, linear propagators grounded in the assumptions of the Koopman operator^{71–75}, reduced basis space obtained through neural networks⁷⁶ or a combination of proper orthogonal decomposition and neural networks⁶⁵, more recently spatial attention mechanism^{77,78} and temporal attention mechanism¹⁷, recurrent Multilayer Perceptrons⁴², state-space model⁷⁹ or continuous dynamics model^{80,81} based on neural Ordinary Equations (ODEs)⁸². In this work, we propose to first train an autoencoder to embed and compress inputs into the latent space, and then employ a Markovian propagator to learn the dynamics of the time-dependent system within this latent space (Figure 1). A detailed schematic for the model architecture used in this work is provided in the Appendix Figure 8.

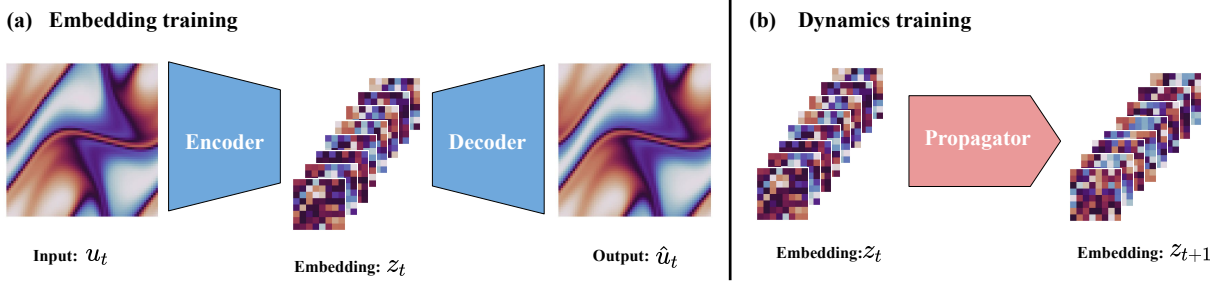


Figure 1: (a) An autoencoder is trained to project the input field to latent field with much coarser discretization. (b) A neural network is trained to predict the latent field at different time steps autoregressively.

3 Methodology

3.1 Problem definition

We are interested in solving time-dependent PDEs of the following form:

$$\frac{\partial u(\mathbf{x}, t)}{\partial t} = F(u(\mathbf{x}, t), t, \theta), \quad \mathbf{x} \in \Omega, t \in [0, T] \quad (1)$$

$$u(\mathbf{x}, 0) = u_0(\mathbf{x}), \quad \mathbf{x} \in \Omega, \quad (2)$$

where T denotes the time horizon, Ω the spatial domain, θ are system parameters such as external forcing magnitude, and some boundary condition for $\mathbf{x} \in \partial\Omega$ is provided *a priori* where $\partial\Omega$ denotes the boundary of the domain. To solve this initial value problem, we assume the system is Markovian such that $\frac{\partial u(\mathbf{x}, t)}{\partial t} = F(u(\mathbf{x}, t), \theta)$, parameters θ are time-invariant, and a neural network is trained to approximate the following time-discretized mapping:

$$u(\mathbf{x}, t + \Delta t) = \mathcal{A}(u(\mathbf{x}, t)), \quad (3)$$

with a fixed Δt , and the system is assumed to be Markovian such that $u(\mathbf{x}, t + 2\Delta t) = \mathcal{A}(\mathcal{A}(u(\mathbf{x}, t)))$.

In practice, the function of interest at a particular time step $u(\cdot, t)$ is sampled on a m -point discretization grid D . For a hierarchical model like U-Net, the grid will be altered internally between different layers and the mapping \mathcal{A} is a composition of a sequence of mapping $\{\mathcal{A}_0, \dots, \mathcal{A}_l\}$ which are approximated on grids $\{D_0, \dots, D_l\}$ with $D_0 = D$ and the number of grid points $m_l < m_{l-1} < \dots < m_0$. In contrast to the aforementioned hierarchical model, we propose to learn \mathcal{A} only on the coarsest grid D_l .

3.2 Autoencoder for discretized field's dimensionality reduction

One of the most straightforward ways to project the function from the original grid to a coarser grid is through interpolation (*e.g.*, bicubic interpolation). However, interpolation can result in significant information loss about the function, as a coarser grid can only evaluate a limited bandwidth and cannot distinguish frequencies that are higher than the Nyquist frequency. To achieve a less lossy compression of the input, we train a non-linear encoder network ϕ to project the input into latent space when coarsening its spatial grid. In the meantime, we train the decoder network ψ to recover the input from the latent embedding that are represented on the coarse grid. The goal of training these two networks is to achieve data compression without too much loss of information such that their composition approximates

an identity mapping: $I \approx \psi \circ \phi$ by minimizing the following lost function:

$$L_{\text{AE}} = C(\psi(\phi(u)), u), \quad (4)$$

where $C(\cdot, \cdot)$ is a distance function which we choose as \mathcal{L}^2 norm for all the systems. After the encoder and decoder network ϕ, ψ are trained, we fix their weights and train another propagator network γ to predict the dynamics of the system: $z_{t+1} = \gamma(z_t)$, where $z_t = \phi(u_t)$, $z_{t+1} = \phi(u_{t+1})$. We empirically observe that training the autoencoder and dynamics propagator separately is crucial for final prediction accuracy (for more details we refer the reader to Section 8 in the supplementary information).

Algorithm 1 First-stage training of encoder and decoder

- 1: **Input:** Training dataset $\{u_1^{(i)}, u_2^{(i)}, \dots, u_T^{(i)}\}_{i=1}^N$, encoder network $\phi(\cdot)$, decoder network $\psi(\cdot)$, distance function $C(\cdot, \cdot)$, total optimization steps K .
 - 2: Initialize ϕ, ψ randomly, set $Iter = 1$.
 - 3: **for** $Iter < K$ **do**
 - 4: Sample a random snapshot $u_t^{(i)}$ from the dataset, where $t \sim \text{Uniform}(\{1, 2, \dots, T\})$
 - 5: Reconstruct the data with autoencoder: $\hat{u}_t^{(i)} = \psi(\phi(u_t^{(i)}))$
 - 6: Compute reconstruction loss: $L_{\text{AE}} = C(\hat{u}_t^{(i)}, u_t^{(i)})$
 - 7: Take gradient descent step based on: $\nabla_{\psi} L_{\text{AE}}, \nabla_{\phi} L_{\text{AE}}$
 - 8: $Iter \leftarrow Iter + 1$
 - 9: **end for**
 - 10: **Output:** Trained encoder ϕ and decoder ψ .
-

Algorithm 2 Second-stage training of the dynamics propagator

- 1: **Input:** Training dataset $\{u_1^{(i)}, u_2^{(i)}, \dots, u_T^{(i)}\}_{i=1}^N$, trained encoder/decoder ϕ, ψ , distance function $C(\cdot, \cdot)$, total optimization steps K , training rollout horizon L .
 - 2: Encode the training dataset into a mesh-reduced latent space: $\{z_1^{(i)}, z_2^{(i)}, \dots, z_T^{(i)}\}_{i=1}^N$, where $z_t^{(i)} = \phi(u_t^{(i)})$. Initialize the propagator network γ randomly, set $Iter = 1$.
 - 3: **for** $Iter < K$ **do**
 - 4: Sample a chunk of consecutive frames with temporal length $L + 1$ from the dataset: $\{z_t^{(i)}, z_{t+1}^{(i)}, \dots, z_{t+L}^{(i)}\}$, where $t \sim \text{Uniform}(\{1, 2, \dots, T - L\})$
 - 5: Initialize $s = t$, $\hat{z}_s^{(i)} \leftarrow z_s^{(i)}$
 - 6: **while** $s < L$ **do**
 - 7: Perform next step prediction: $\hat{z}_{s+1}^{(i)} = \gamma(\hat{z}_s^{(i)})$
 - 8: $s \leftarrow s + 1$
 - 9: **end while**
 - 10: Compute dynamics prediction loss: $L_{\text{DYN}} = C\left(\{\hat{z}_s^{(i)}\}_{s=t+1}^{t+L}, \{z_s^{(i)}\}_{s=t+1}^{t+L}\right)$
 - 11: Take gradient descent step on: $\nabla_{\gamma} L_{\text{DYN}}$
 - 12: $Iter \leftarrow Iter + 1$
 - 13: **end for**
 - 14: **Output:** Trained propagator γ .
-

In this work, we exploit the uniform grid structure, so that the majority of the autoencoder can be parameterized with convolutional neural networks (CNN) which have been shown to be effective for compressing imagery data^{59,60,83}. On top of the CNN modules, we also introduce self-attention layers⁸⁴ near the bottleneck for better capturing long-range dependency in the field, which is beneficial for image synthesis tasks^{16,60,85}. Given the i -th input feature vector $u_i \in \mathbb{R}^{d_c}$ with channel size d_c , the (self-)attention can be defined as:

$$u'_i = \sum_{j=1}^m \alpha_{ij} v_j, \quad \alpha_{ij} = \frac{\exp(q_i \cdot k_j / \sqrt{d_c})}{\sum_{s=1}^m \exp(q_i \cdot k_s / \sqrt{d_c})}, \quad (5)$$

where: $q_i = W_q u_i$, $k_i = W_k u_i$, $v_i = W_v u_i$ respectively, and $W_q, W_k, W_v \in \mathbb{R}^{d_c \times d_c}$ are learnable weights. Attention is also closely related to the learnable kernel integral³⁶:

$$u_{l+1}(x) = \int_{\Omega} \kappa(x, y) u_l(y) dy, \quad (6)$$

where u_{l+1} is the output function, u_l is the input function with respect to l -th layer, and $\kappa(\cdot)$

is the kernel parameterized by the dot product attention. The above learnable kernel integral is often used as the basic building block for learning mappings between function spaces. It can be parameterized with attention by using (5) to compute the κ under some discretization of the domain, which have been studied in several prior works^{8,35,42,43,86,87}. In the bottleneck, we use standard self-attention while for higher-resolution feature map we opt for axial factorized attention⁸⁷ which has superior computational efficiency on multi-dimensional problems.

3.3 Baseline neural PDE solver

Fourier neural operator The spectral convolution layer is first proposed in the Fourier Neural Operator (FNO)² as a parameterization of the learnable kernel integral³⁶. It applies a discrete Fourier transform to the input and then multiplies the k -lowest modes with learnable complex weights. Given input function u_l , the spectral convolution computes the kernel integral as follows:

$$u_{l+1}(x) = \int_{\Omega} \kappa(x-y) u_l(y) dy = \sum_{\xi_1=0}^{\xi_1^{\max}} \dots \sum_{\xi_n=0}^{\xi_n^{\max}} \mathbf{W}_j \mathbf{c}_j \mathbf{f}_j(x), \quad (7)$$

where \mathbf{f}_j is the j -th ($j := (\xi_1, \xi_2, \dots, \xi_n)$) Fourier basis function: $\mathbf{f}_j(x) = \exp(2i\pi \sum_d \frac{x_d \xi_d}{m_d})$, $\xi_d \in \{0, 1, \dots, m_d\}$ with m_d being the resolution along the d -th dimension, x_d being the coordinate for d -th dimension, and $\mathbf{c}_j = \langle u_l, \mathbf{f}_j \rangle$ denotes the inner product between an input function and the Fourier series, $\mathbf{W} \in \mathbb{C}^{(\xi_1^{\max} \times \xi_2^{\max} \times \dots \times \xi_n^{\max}) \times d_c \times d_c}$ is the learnable weight with frequency mode of the input at i -th dimension truncated up to ξ_i^{\max} . Unlike the CNN layer, spectral convolution is able to capture multi-scale features that correspond to different frequencies within a single layer. It is also computationally efficient on a uniform grid as the c_j can be computed via fast Fourier Transformation (FFT). In the original FNO, the update scheme at each layer is designed as follows:

$$u_{l+1} = \sigma(K(u_l) + w(u_l)), \quad (8)$$

where w is a learnable linear transformation and K is the spectral convolution as defined in (7). Subsequent FNO^{29,50,51} works have shown that it is usually beneficial to use an update scheme similar to a standard Transformer with a skip connection^{84,88}:

$$\begin{aligned} u' &= K(\tilde{u}_l) + u_l, \\ u_{l+1} &= \text{FFN}(\tilde{u}') + u', \end{aligned} \tag{9}$$

where $\text{FFN}(\cdot)$ is a two-layer point-wise MLP (also known as a feed-forward network in Transformer literature), $\tilde{\diamond}$ denotes a feature map \diamond that is normalized, common choices of normalization include instance normalization⁸⁹ and layer normalization⁹⁰. We use instance normalization for u_l and layer normalization for u' . Such architectural design is usually called a "mixer" in the computer vision literatures (e.g. Conv-Mixer⁹¹, MLP-Mixer⁹²), so we refer to this variant of FNO as FNO-Mixer in the rest of the paper.

UNet In the previous section we have introduced an autoencoder for projecting a discretized field to a coarse grid and learning the dynamics of the system on the coarsest grid. As an alternative to operating on the coarsest grid, we also investigate learning the dynamics on multiple discretization levels. This can be done by establishing a skip connection between every level in the encoder and decoder, from the input grid D_0 to the coarsest grid D_l , resulting in a standard U-Net architecture.

3.4 Conditioning

Since we adopt a Markovian setting across all the experiments, there is no context for a model to infer dynamical property of the system such as the oscillation frequency of the external forcing. To modulate the prediction of neural networks based on the conditioning information, we investigate conditioning strategies that are often used in image-related tasks and introduced to PDE problems recently in Gupta and Brandstetter⁹. The system parameter $\theta \in \mathbb{R}$ (in our problem we have only a single scalar parameter but it is straightforward to

extend this formulation to multi-variable parameter) are first projected to a high-dimensional embedding $\mathbf{q} \in \mathbb{R}^{d_f}$ using the sinusoidal projection from Vaswani et al.⁸⁴ followed by a feed-forward network:

$$q' = \left[\cos(\theta), \sin(\theta), \cos\left(\frac{\theta}{10000^{2/d}}\right), \sin\left(\frac{\theta}{10000^{2/d}}\right), \dots, \cos\left(\frac{\theta}{10000^{2(d-1)/d}}\right), \sin\left(\frac{\theta}{10000^{2(d-1)/d}}\right) \right],$$

$$q = \text{FFN}(q'),$$
(10)

where d is the a hyperparameter of hidden dimension and $d_f = 2d$. Below we will illustrate how to modulate different layers with the conditioning parameter q .

Conditioning for a feed-forward network We use a strategy similar to "AdaGN" proposed in Nichol and Dhariwal⁹³ to modulate the input to the feed-forward network. Given input u_l , we inject the conditioning information q by doing an element-wise multiplication before processing it with a feed-forward network FFN_l :

$$u'_l = \text{FFN}_{\text{cond}}(q) \odot u_l,$$

$$u_{l+1} = \text{FFN}_l(u'_l) + u_l.$$
(11)

Conditioning for a spectral convolution layer We adopt the frequency domain conditioning strategy proposed in Gupta and Brandstetter⁹. The conditioning embedding q first projects to a complex embedding vector $\hat{\mathbf{q}} \in \mathbb{C}^{(\xi_1^{\max} \times \xi_2^{\max} \times \dots \times \xi_n^{\max})}$: $\hat{\mathbf{q}} = qW_{\text{real}}^l + iqW_{\text{imag}}^l$, where $W_{\text{real}}^l, W_{\text{imag}}^l \in \mathbb{R}^{c \times (\xi_1^{\max} \times \xi_2^{\max} \times \dots \times \xi_n^{\max})}$ are learnable weights. Then the conditioned version of (7) is defined as:

$$u_{l+1}(x) = \sum_{\xi_1=0}^{\xi_1^{\max}} \dots \sum_{\xi_n=0}^{\xi_n^{\max}} \hat{\mathbf{q}}_j \mathbf{W}_j \mathbf{c}_j \mathbf{f}_j(x), \quad j := (\xi_1, \xi_2, \dots, \xi_n).$$
(12)

Conditioning for a convolution block For the conditioning of convolutional layers in the autoencoder and UNet, we following the conditioning strategy that is widely used in diffusion models¹⁶, which amounts to adding the conditioning embedding to the input of

convolution layer:

$$\begin{aligned} u'_l &= u_l + \text{FFN}_{\text{cond}}(q), \\ u_{l+1} &= \text{Conv}_l(u'_l) + u_l. \end{aligned} \tag{13}$$

4 Experiments

We test out the proposed model on three types of time-dependent PDE problems. In addition, we use the model to predict a system with a varying parameter (oscillation frequency) for a two-phase flow.

4.1 Problems

Navier-Stokes equation The 2D Navier-Stokes equation we consider is the 2D flow dataset proposed in Li et al.², which is based on 2D Navier-Stokes equation with a vorticity formulation. The vorticity form reads as:

$$\begin{aligned} \frac{\partial \omega(\mathbf{x}, t)}{\partial t} + \mathbf{u}(\mathbf{x}, t) \cdot \nabla \omega(\mathbf{x}, t) &= \nu \nabla^2 \omega(\mathbf{x}, t) + f(\mathbf{x}), \quad \mathbf{x} \in (0, 1)^2, t \in (0, T], \\ \nabla \cdot \mathbf{u}(\mathbf{x}, t) &= 0, \quad \mathbf{x} \in (0, 1)^2, t \in [0, T], \\ \omega(\mathbf{x}, 0) &= \omega_0(\mathbf{x}), \quad \mathbf{x} \in (0, 1)^2, \end{aligned} \tag{14}$$

where ω denotes vorticity: $\omega := \nabla \times u$, the initial condition ω_0 is sampled from the Gaussian random field: $\mathcal{N}(0, 7^{3/2}(-\Delta + I)^{-2.5})$, the boundary condition is periodic: $u([x_1 + 1, x_2], t) = u[x_1, x_2], t)$, $u([x_1, x_2 + 1], t) = u([x_1, x_2], t)$, $\forall x_1, x_2 \in (0, 1)$, the viscosity coefficient ν is $1e-4$ (dimensionless, corresponds to a Reynolds number of roughly 200) and the forcing term is defined as: $f(\mathbf{x}) = 0.1(\sin 2\pi(x_1 + x_2) + \cos 2\pi(x_1 + x_2))$. We are interested in learning to simulate the system (by predicting vorticity) from $t = 5$ to $t = 35$ seconds. The reference numerical simulation data is generated via the pseudo-spectral method. The dataset contains 1000 trajectories where we use 900 for training and 100 for testing.

Shallow water equation We consider the 2D shallow water equation that is proposed in Gupta and Brandstetter⁹, which use the SpeedyWeather library¹ to perform the numerical simulation. The equation is defined as:

$$\begin{aligned}\frac{\partial \omega}{\partial t} + \nabla \cdot (\mathbf{u}(\omega + f)) &= F_\omega + \nabla \times \mathbf{F}_\mathbf{u} + (-1)^{n+1} \nu \nabla^{2n} \omega, \\ \frac{\partial \mathcal{D}}{\partial t} - \nabla \times (\mathbf{u}(\omega + f)) &= F_\mathcal{D} + \nabla \cdot \mathbf{F}_\mathbf{u} - \nabla^2 (\tfrac{1}{2}(u^2 + v^2) + g\eta) + (-1)^{n+1} \nu \nabla^{2n} \mathcal{D}, \\ \frac{\partial \eta}{\partial t} + \nabla \cdot (\mathbf{u}h) &= F_\eta,\end{aligned}\quad (15)$$

where ω is the vorticity, g is the gravitational acceleration, f is the Coriolis parameter, η is the interface height (which can be interpreted as the pressure term), h is dynamic layer thickness, $\mathcal{D} = \nabla \cdot \mathbf{u}$ is the velocity divergence, $F_\zeta, F_\mathcal{D}, F_\eta, \mathbf{F}_\mathbf{u} = (F_u, F_v)$ are different types of forcing terms (we refer reader to the official documentation of SpeedyWeather for more details). The dataset contains 1400 training trajectories and 1400 testing trajectories, each trajectory is of length 21 days (we sample each frame with an interval of 12h).

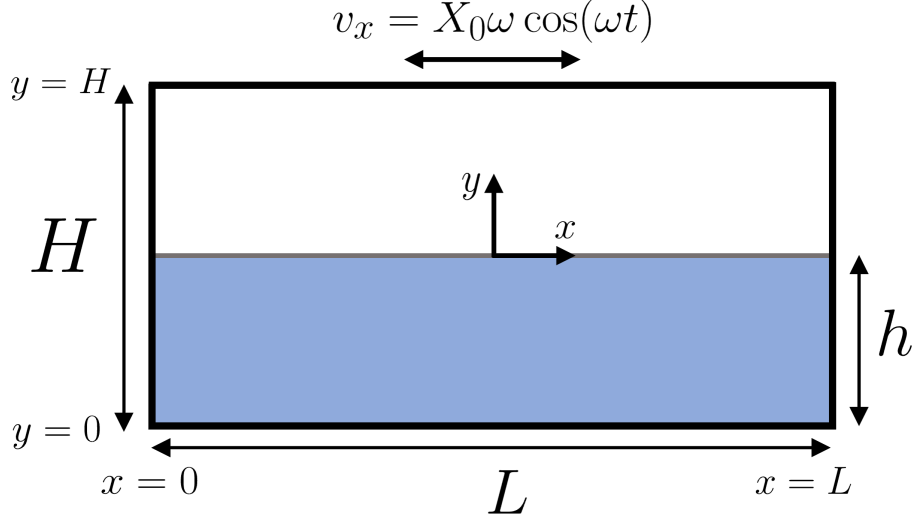


Figure 2: Description of the tank sloshing system

¹<https://github.com/SpeedyWeather/SpeedyWeather.jl>

Tank sloshing We consider the multi-phase problem of liquid sloshing in a partially filled 2D rectangular container subject to external perturbation. The motion of the liquid in the container is assumed to be incompressible, viscous, and turbulent, and we subject the container to a forced sinusoidal horizontal oscillation at a specific frequency ω and amplitude X_0 . No-slip boundary conditions are applied at the boundaries of the container. Therefore, we use the Reynolds-Averaged Navier-Stokes (RANS) equations⁹⁴ to model the large scale mean fluid flow, and a turbulence closure model to describe the Reynolds stress induced by the velocity fluctuation terms. The Reynolds-Averaged continuity and Navier-Stokes equations are defined as:

$$\begin{aligned}
\nabla \cdot (\rho_m \bar{\mathbf{u}}) &= 0 \\
\frac{\partial(\rho_m \bar{\mathbf{u}})}{\partial t} + \nabla \cdot (\rho_m \bar{\mathbf{u}} \bar{\mathbf{u}}) &= -\nabla \bar{p} + \nabla \cdot [\mu_{e,m}(\nabla \bar{\mathbf{u}} + (\nabla \bar{\mathbf{u}})^T) - \frac{2}{3}\rho_m \kappa \mathbf{I}] + \rho_m \mathbf{g} + \rho_m \mathbf{f}_s \\
\mu_{e,m} &= (1 - \alpha)\mu_g + \alpha\mu_l + \mu_t \\
\rho_m &= (1 - \alpha)\rho_g + \alpha\rho_l \\
\bar{\mathbf{u}}_{\Gamma_1} &= 0 \\
\bar{\mathbf{u}}_{\Gamma_2} \cdot \hat{\mathbf{n}} &= 0
\end{aligned} \tag{16}$$

where $\alpha(\mathbf{x}, t)$ is the phase fraction of liquid, Γ_1 is the boundary of the container, \mathbf{I} is the identity tensor. Additionally, \mathbf{g} is the gravitational force, κ is the turbulent kinetic energy, Γ_2 is the boundary between the liquid and gas phases, and ρ_m is the mixture density accounting for the weighted contributions of the gas density, ρ_g and the liquid density, ρ_l . To model the turbulent stress, we use the two equation $k - \epsilon$ model to describe the conservation of turbulent kinetic energy, k , and the rate of dissipation of turbulent kinetic energy, ϵ ⁹⁵ (more details are provided in the supplementary information). The effective mixture viscosity is given by $\mu_{e,m}$, which accounts for the contributions of the turbulent viscosity, μ_t , and the weighted contributions of the gas viscosity μ_g and the liquid viscosity μ_l . μ_t is defined in terms of k and ϵ according to Equation 21. The container motion is prescribed as an acceleration term,

\mathbf{f}_s , where \mathbf{f}_s is given by

$$\mathbf{f}_s = -X_0\omega^2 \sin(\omega t)\mathbf{e}_1 \quad (17)$$

in which X_0 is the amplitude of the container motion, ω is the angular frequency of the container oscillation, ρ is the density of the fluid within the container, and \mathbf{e}_1 is the horizontal unit vector.

The Volume of Fluid method is implemented to resolve the interface behavior between phases. To do so, α is defined to represent the volume fraction of liquid within each mesh element. The advection equation for α is defined as

$$\frac{\partial \alpha}{\partial t} + \nabla \cdot (u\alpha) = 0 \quad (18)$$

ANSYS[®] FLUENT (v2023R2, ANSYS, Inc., Canonsburg, PA) is used to create datasets for two experiments. In the first experiment, 248 sloshing cases are created at angular frequencies ranging from $\omega = 1.0$ rad/s to $\omega = 9.9$ rad/s. The container is initialized at rest before the forced oscillation is applied for a duration of 8.0 s. Referring to (Figure 2) and Equation (16), we take $L = 1.2m$, $H = 0.6m$, $\mu_l = 1 \times 10^{-3}$ Pa · s, $\rho_l = 9.98 \times 10^2$ kg m⁻³, $\mu_g = 1.8 \times 10^{-5}$ Pa · s, and $\rho_g = 1.23$ kg m⁻³. We let 40% of the container volume be occupied by liquid and the remainder be occupied by gas. The intent is to model an air-water system. In the second experiment, the frequency is held constant at 3 rad/s and the initialized liquid level is varied from 10% to 90% of the total height of the container. These experiments are configured to avoid high-speed jet formation events caused by fluid impact with the container roof, and to span multiple distinct regimes of the sloshing behavior.^{96,97}

4.2 Implementation

In this section, we list a brief summary of the experiment settings and for further details we refer reads to the Section 6 in the Appendix.

LNS Autoencoder The encoder and decoder are mainly built upon convolutional layers. Internally they comprise a stack of downsampling/upsampling blocks, where each block downsamples/upsamples the spatial resolution by a factor of 2. Each block contains a residual convolution block and a downsampling/upsampling layer. Self-attention layers are applied to the first two lowest resolution in the decoder part. Across all problems, the latent grid is 8 times coarser than the original grid. For the 2D Navier-Stokes problem, we set the latent resolution to 8×8 (original resolution: 64×64) and the latent dimension to 16. For the two-phase flow problem, the latent resolution is 7×15 (original resolution: 61×121) and the latent dimension is 64. For the shallow-water equation, the latent resolution is 12×24 (original resolution: 96×192), with latent dimension also equals to 64.

LNS Propagator We use a simple residual network⁸⁸ to forecast the forward dynamics in the latent space, where each residual block contains three convolution layers with 3×3 convolution kernels and followed with a two-layer MLP. We employ dilated convolution for the middle convolution layer to capture multi-scale interaction. For the 2D Navier-Stokes problem, we use 3 residual blocks with a network width 128. For other problems, we use 4 residual blocks with a network width 128 given the increased complexity of the problem.

Baselines For FNO and FNO-Mixer, we use a layer of 4 and hidden dimension of 64, the modes used in different problems are marked as subscript in each result table, e.g. $\text{FNO}_{\xi_y, \xi_x}$ means using ξ_y modes in y -direction and ξ_x modes in x -direction. For UNet in each problem, we use the same architecture as the autoencoder in LNS but use a skip connection at every level between the encoder and decoder.

Training We first train the autoencoder by minimizing the relative L^2 reconstruction loss with a constant learning rate $3e - 5$ using batch size of 32/64 depending on the size of the system. We then train the propagator by minimizing the mean squared error between predicted embeddings and embed reference data for another 150k iterations with a learning

rate of $5e-4$ and a cosine annealing schedule. For other models that operate on a full-order discretized space, we train it with a learning rate of $5e-4$ and a cosine annealing scheduling to minimize the relative L^2 prediction loss. During training, we also rollout the model to improve long-term stability. On the Navier-Stokes case, we rollout for 2 steps during training and on tank sloshing problem, we rollout for 5 steps during training. For these two systems, we find that further increasing the training rollout steps does not improve the testing performance significantly. On the shallow water equation, we observe that a longer rollout during training can greatly improve the the stability during training.

4.3 Results

In this section we will present the numerical results of different neural PDE solvers. We use relative L^2 norm between the predicted sequence \hat{u} to the ground truth (GT) u to measure the quantitative accuracy:

$$\text{Error} = \sqrt{\frac{\sum_{t=1}^T \sum_{i=1}^N (\hat{u}_{i,t} - u_{i,t})^2}{\sum_{t=1}^T \sum_{i=1}^N u_{i,t}^2}}, \quad (19)$$

with temporal discretization points $t \in 0, 1, \dots, T$ where T denotes the temporal horizon, and spatial discretization points $i \in 0, 1, \dots, N$ where N denotes the total number of spatial grid points. We also benchmark the computational cost of each model by profiling its training wall-clock time per iteration and peak GPU memory allocated.

As shown in Table 1, 2, 3 and Figure 3, 4 we observe that all models can reach an error around or less than 15% on the Navier-Stokes and tank sloshing problems. The best performing model varies case by case. FNO-Mixer shows a consistent improvement over FNO on these problems with increased computational cost. Notably, LNS achieves comparable results with UNet on these cases with greatly reduced computational cost. In addition, for the tank sloshing problem with varying frequency, all models can learn to predict the dynamics based on the conditioning parameter as demonstrated in Table 3.

On more chaotic system - the shallow water equation, the performance discrepancy becomes more significant (see Table 4 and Figure 5, 6). For UNet, despite its good prediction at the initial stage (green line in the Figure 7)), it quickly blows up during the middle of the simulation and artifacts can be observed from the results. In general all the models are not able to maintain a stable long-term simulation (ending error greater than 100% as shown in Figure 7) with only limited training rollout steps (5 steps). This blow-up error arises from the fact that these neural solvers do not have stability guarantee. The multi-step training target with backprop-through-time can effectively alleviate this. As given model's prediction $\hat{u}_{t+1} = \mathcal{A}_\theta(u_t) = u_{t+1} + \epsilon_t$ where ϵ_t is the prediction error of network at time step t , a multi-step rollout loss (e.g. using L^2 norm): $\|\mathcal{A}_\theta(\mathcal{A}_\theta(\dots\mathcal{A}_\theta(u_{t+1} + \epsilon_t))) - u_{t+L}\|_2$ requires the model remain stable under perturbation ϵ_t . However, the computational cost increase linearly with respect to the rollout steps. Thanks to the highly compressed latent vector field in LNS, rolling out for more steps is much more affordable than models that operate on full-order space. Training LNS with training rollout steps up to 20 is still highly efficient. As shown in the result, the longer training rollout steps greatly improves different models' stability. LNS trained with 20 rollout steps successfully maintain stable throughout the whole simulation and outperforms FNO and FNO-Mixer by a notable margin (Figure 7). It is worth noting that when training with more rollout steps, the model tends to trade-off next-step prediction accuracy for stability. At the beginning of simulation, LNS-5 and LNS-10 exhibit lower error compared to LNS-20. We hypothesize the major reason the data distribution in each training batches is affect by the rollout steps. The model with longer training rollout steps will observe more samples that are generated from its own prediction, whereas model trained with fewer rollout steps sees more samples from the dataset. At earlier time step during testing, the input will be much closer to the ground truth data distribution p_{data} and gradually shift towards p_{pred} due to error accumulation, thus the model that has trained with longer rollout tend to perform slightly worse at the beginning.

Table 1: (2D) Navier-Stokes equation with vorticity formulation. The computational runtime is benchmarked with a batch size of 32 on a RTX3090 GPU.

Model	Rollout error	Time per iter (s)	Peak Memory (Gb)
FNO _{16,16}	0.136	0.043	3.89
FNO-Mixer _{16,16}	0.061	0.055	4.91
UNet	0.042	0.126	5.96
LNS (Ours)	0.074	0.064+0.017	4.43+2.97

Table 2: Tank sloshing - Varying height. The computational runtime is benchmarked with a batch size of 32 on a RTX3090 GPU.

Model	Rollout error			Time per iter (s)	Peak Memory
	\mathbf{u}	p	F		
FNO _{16,32}	0.171	0.008	0.009	0.20	7.92
FNO-Mixer _{16,32}	0.119	0.006	0.008	0.25	13.32
UNet	0.101	0.004	0.006	0.33	16.52
LNS (Ours)	0.085	0.006	0.010	0.054+0.029	4.90+3.78

Table 3: Tank sloshing - Varying frequency (Conditional prediction). The computational runtime is benchmarked with a batch size of 32 on a RTX3090 GPU.

Model	Rollout error			Time per iter (s)	Peak Memory (Gb)
	\mathbf{u}	p	F		
FNO _{16,32}	0.042	0.002	0.004	0.21	9.29
FNO-Mixer _{16,32}	0.030	0.002	0.003	0.27	14.38
UNet	0.037	0.004	0.002	0.34	16.94
LNS (Ours)	0.041	0.006	0.004	0.054+0.040	4.90+4.18

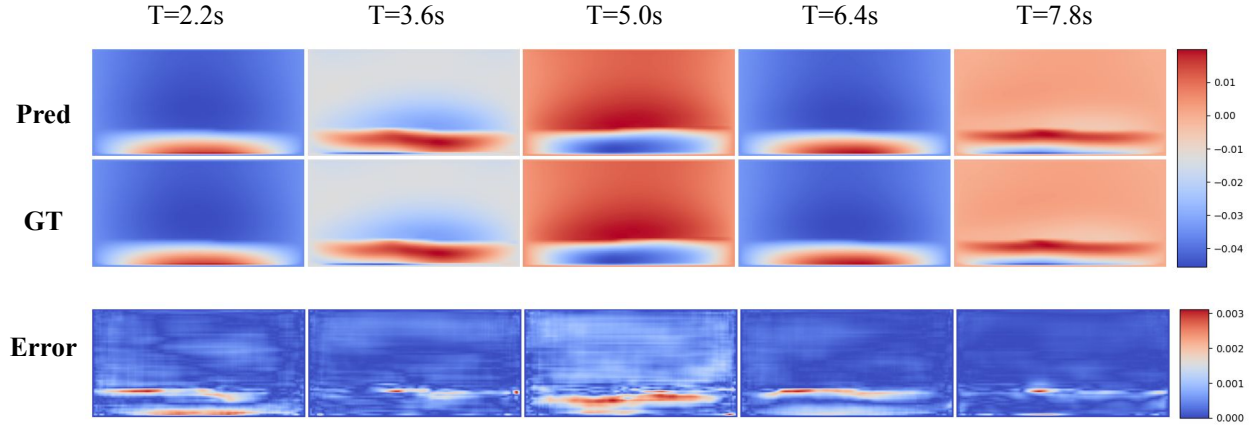


Figure 3: Tank Sloshing: Sample prediction of x component of the velocity field \mathbf{u} on *varying height dataset* with liquid surface height: $h = 25\%$. Unit: m/s .

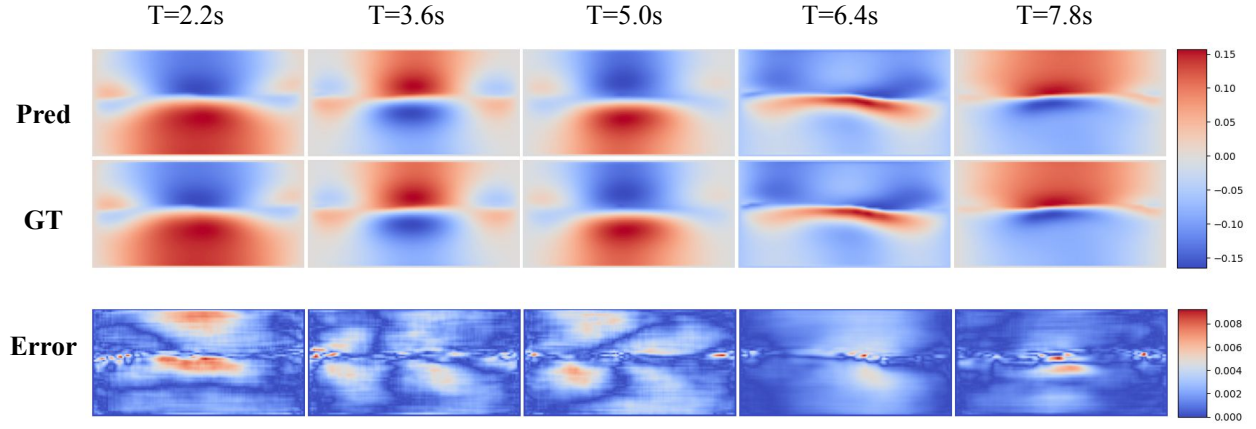


Figure 4: Tank Sloshing: Sample prediction x component of the velocity field \mathbf{u} on *varying frequency dataset* with oscillation frequency: $\omega = 7.12$ rad/s. Unit: m/s .

Table 4: Shallow water equation. The computational runtime is benchmarked with a batch size of 32 on a A6000 GPU. ”-” indicates this training setting is too computationally expensive to carry out.

Model	Training Rollout steps	Rollout error		Time per iter (s)	Peak Memory (Gb)		
		\mathbf{u}	η				
FNO _{16,32}	5	0.527	0.558	0.42	14.58		
	10	0.214	0.307	0.87	26.98		
	20	-	-	-	-		
FNO-Mixer _{16,32}	5	0.668	0.656	0.54	25.10		
	10	0.271	0.336	1.09	46.19		
	20	-	-	-	-		
UNet	5	0.931	1.180	1.13	36.87		
	10	-	-	-	-		
	20	-	-	-	-		
LNS (Ours)	5	0.736	0.758	0.10	4.05		
	10	0.198	0.199	0.33+	0.19	17.39+	4.76
	20	0.132	0.113		0.36		6.42

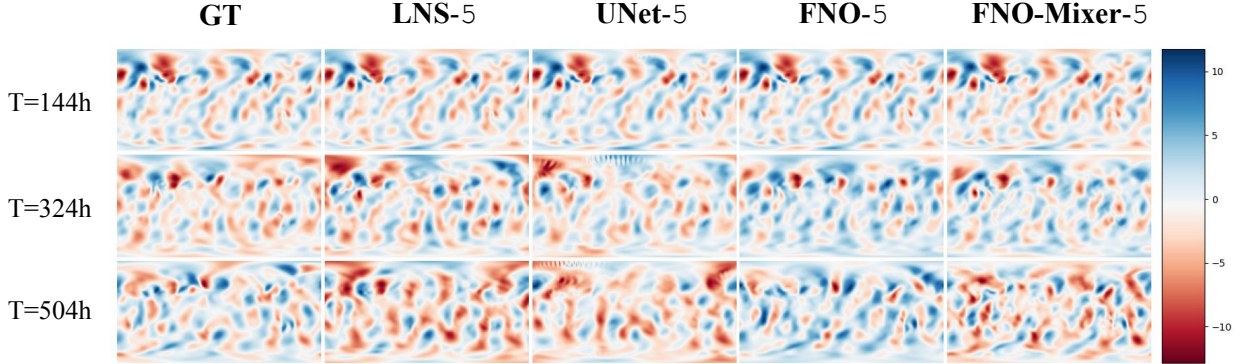


Figure 5: Shallow Water: Comparison on models’ predicted y –component of \mathbf{u} with 5 training rollout steps. UNet’s prediction exhibits notable artifacts after certain time steps. Unit: m/s .

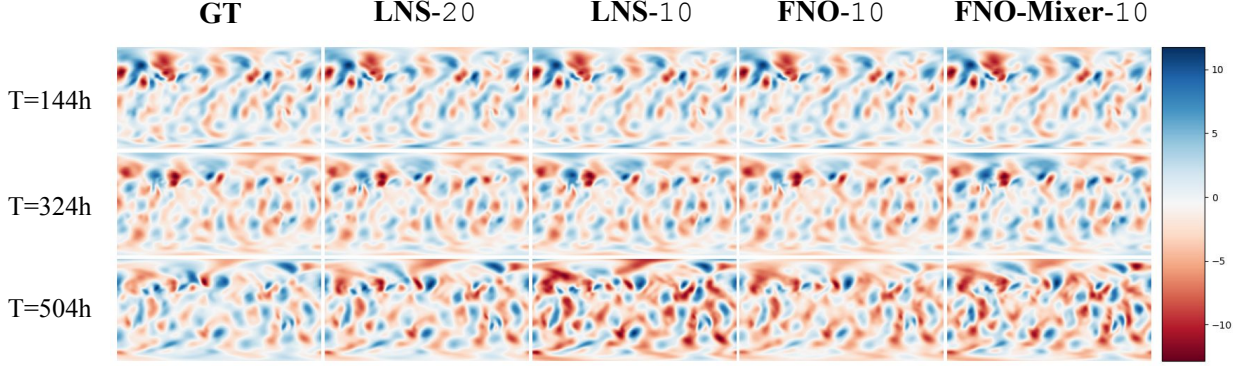


Figure 6: Shallow Water: Comparison on models' predicted y -component of \mathbf{u} with longer training rollout.

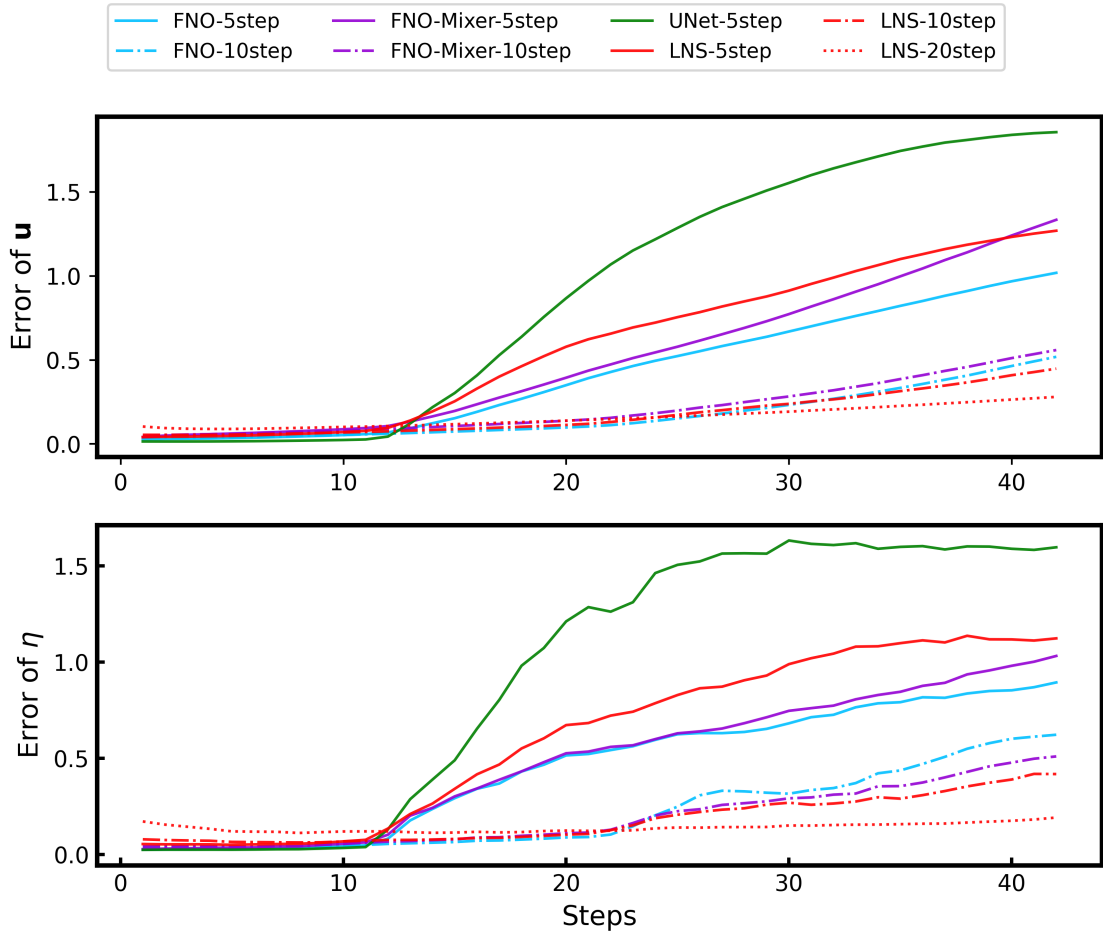


Figure 7: Comparison of rollout error trend of different models on the shallow water equation, the Δt for each step is 12h. The step number after each model's name indicates its training rollout steps.

5 Conclusion

In this work, we propose a new data-driven framework for predicting time-dependent PDEs and investigate different kinds of neural PDE solvers. We show that training the temporal model in the mesh-reduced space improves the computational efficiency and is beneficial for problems that feature latent dynamics distributed on a low-dimensional manifold. It also opens up the possibility for training model with longer backprop-through-time horizon, which can significantly improve models’ stability. The observation in this study is also in alignment with the recent success of a series of image synthesis models that learn the generative model in the latent space instead of pixel space^{59,60,98}. As this work only considers uniform meshes, an interesting future direction would be the extension to arbitrary meshes and geometries.

References

- (1) Raissi, M.; Perdikaris, P.; Karniadakis, G. E. Physics-informed neural networks: A deep learning framework for solving forward and inverse problems involving nonlinear partial differential equations. *Journal of Computational physics* **2019**, *378*, 686–707.
- (2) Li, Z.; Kovachki, N. B.; Azizzadenesheli, K.; Liu, B.; Bhattacharya, K.; Stuart, A.; Anandkumar, A. Fourier Neural Operator for Parametric Partial Differential Equations. International Conference on Learning Representations. 2021.
- (3) Lu, L.; Jin, P.; Pang, G.; Zhang, Z.; Karniadakis, G. E. Learning nonlinear operators via DeepONet based on the universal approximation theorem of operators. *Nature Machine Intelligence* **2021**, *3*, 218–229.
- (4) Sanchez-Gonzalez, A.; Godwin, J.; Pfaff, T.; Ying, R.; Leskovec, J.; Battaglia, P. Learning to simulate complex physics with graph networks. International conference on machine learning. 2020; pp 8459–8468.

- (5) Pfaff, T.; Fortunato, M.; Sanchez-Gonzalez, A.; Battaglia, P. Learning Mesh-Based Simulation with Graph Networks. *International Conference on Learning Representations*. 2021.
- (6) Brandstetter, J.; Worrall, D. E.; Welling, M. Message Passing Neural PDE Solvers. *International Conference on Learning Representations*. 2022.
- (7) Stachenfeld, K.; Fielding, D. B.; Kochkov, D.; Cranmer, M.; Pfaff, T.; Godwin, J.; Cui, C.; Ho, S.; Battaglia, P.; Sanchez-Gonzalez, A. Learned Simulators for Turbulence. *International Conference on Learning Representations*. 2022.
- (8) Cao, S. Choose a Transformer: Fourier or Galerkin. *Advances in Neural Information Processing Systems*. 2021; pp 24924–24940.
- (9) Gupta, J. K.; Brandstetter, J. Towards Multi-spatiotemporal-scale Generalized PDE Modeling. *Transactions on Machine Learning Research* **2023**,
- (10) Li, Z.; Kovachki, N.; Azizzadenesheli, K.; Liu, B.; Stuart, A.; Bhattacharya, K.; Anandkumar, A. Multipole graph neural operator for parametric partial differential equations. *Advances in Neural Information Processing Systems*. 2020; pp 6755–6766.
- (11) Wang, R.; Kashinath, K.; Mustafa, M.; Albert, A.; Yu, R. Towards physics-informed deep learning for turbulent flow prediction. *Proceedings of the 26th ACM SIGKDD International Conference on Knowledge Discovery & Data Mining*. 2020; pp 1457–1466.
- (12) Rahman, M. A.; Ross, Z. E.; Azizzadenesheli, K. U-NO: U-shaped Neural Operators. *Transactions on Machine Learning Research* **2023**,
- (13) Thuerey, N.; Weißenow, K.; Prantl, L.; Hu, X. Deep learning methods for Reynolds-averaged Navier–Stokes simulations of airfoil flows. *AIAA Journal* **2020**, *58*, 25–36.
- (14) Pant, P.; Doshi, R.; Bahl, P.; Farimani, A. B. Deep learning for reduced order modelling and efficient temporal evolution of fluid simulations. *Physics of Fluids* **2021**, *33*, 107101.

- (15) Ronneberger, O.; Fischer, P.; Brox, T. U-net: Convolutional networks for biomedical image segmentation. Medical Image Computing and Computer-Assisted Intervention–MICCAI 2015: 18th International Conference, Munich, Germany, October 5-9, 2015, Proceedings, Part III 18. 2015; pp 234–241.
- (16) Ho, J.; Jain, A.; Abbeel, P. Denoising diffusion probabilistic models. Advances in neural information processing systems. 2020; pp 6840–6851.
- (17) Han, X.; Gao, H.; Pfaff, T.; Wang, J.-X.; Liu, L. Predicting Physics in Mesh-reduced Space with Temporal Attention. International Conference on Learning Representations. 2022.
- (18) Geneva, N.; Zabarar, N. Transformers for modeling physical systems. *Neural Networks* **2022**, *146*, 272–289.
- (19) List, B.; Chen, L.-W.; Bali, K.; Thuerey, N. How Temporal Unrolling Supports Neural Physics Simulators. 2024.
- (20) Ummenhofer, B.; Prantl, L.; Thuerey, N.; Koltun, V. Lagrangian Fluid Simulation with Continuous Convolutions. International Conference on Learning Representations. 2020.
- (21) Prantl, L.; Ummenhofer, B.; Koltun, V.; Thuerey, N. Guaranteed conservation of momentum for learning particle-based fluid dynamics. Advances in Neural Information Processing Systems. 2022; pp 6901–6913.
- (22) Li, Z.; Farimani, A. B. Graph neural network-accelerated Lagrangian fluid simulation. *Computers & Graphics* **2022**, *103*, 201–211.
- (23) Löttsch, W.; Ohler, S.; Otterbach, J. Learning the Solution Operator of Boundary Value Problems using Graph Neural Networks. ICML 2022 2nd AI for Science Workshop. 2022.

- (24) Li, Y.; Wu, J.; Tedrake, R.; Tenenbaum, J. B.; Torralba, A. Learning Particle Dynamics for Manipulating Rigid Bodies, Deformable Objects, and Fluids. *International Conference on Learning Representations*. 2019.
- (25) JANNY, S.; Bénéteau, A.; Nadri, M.; Digne, J.; THOME, N.; Wolf, C. EAGLE: Large-scale Learning of Turbulent Fluid Dynamics with Mesh Transformers. *International Conference on Learning Representations*. 2023.
- (26) Rasp, S.; Dueben, P. D.; Scher, S.; Weyn, J. A.; Mouatadid, S.; Thuerey, N. WeatherBench: A Benchmark Data Set for Data-Driven Weather Forecasting. *Journal of Advances in Modeling Earth Systems* **2020**, *12*.
- (27) Nguyen, T.; Brandstetter, J.; Kapoor, A.; Gupta, J. K.; Grover, A. ClimaX: A foundation model for weather and climate. *Proceedings of the 40th International Conference on Machine Learning*. 2023; pp 25904–25938.
- (28) Lam, R. et al. Learning skillful medium-range global weather forecasting. *Science* **2023**, *382*, 1416–1421.
- (29) Kurth, T.; Subramanian, S.; Harrington, P.; Pathak, J.; Mardani, M.; Hall, D.; Miele, A.; Kashinath, K.; Anandkumar, A. Fourcastnet: Accelerating global high-resolution weather forecasting using adaptive fourier neural operators. *Proceedings of the Platform for Advanced Scientific Computing Conference*. 2023; pp 1–11.
- (30) Zhu, M.; Zhang, H.; Jiao, A.; Karniadakis, G. E.; Lu, L. Reliable extrapolation of deep neural operators informed by physics or sparse observations. *Computer Methods in Applied Mechanics and Engineering* **2023**, *412*, 116064.
- (31) Pang, G.; Lu, L.; Karniadakis, G. E. fPINNs: Fractional physics-informed neural networks. *SIAM Journal on Scientific Computing* **2019**, *41*, A2603–A2626.

- (32) Lu, L.; Meng, X.; Mao, Z.; Karniadakis, G. E. DeepXDE: A deep learning library for solving differential equations. *SIAM review* **2021**, *63*, 208–228.
- (33) Cai, S.; Mao, Z.; Wang, Z.; Yin, M.; Karniadakis, G. E. Physics-informed neural networks (PINNs) for fluid mechanics: A review. *Acta Mechanica Sinica* **2021**, *37*, 1727–1738.
- (34) Karniadakis, G. E.; Kevrekidis, I. G.; Lu, L.; Perdikaris, P.; Wang, S.; Yang, L. Physics-informed machine learning. *Nature Reviews Physics* **2021**, *3*, 422–440.
- (35) Kissas, G.; Seidman, J. H.; Guillo, L. F.; Preciado, V. M.; Pappas, G. J.; Perdikaris, P. Learning operators with coupled attention. *The Journal of Machine Learning Research* **2022**, *23*, 9636–9698.
- (36) Kovachki, N.; Li, Z.; Liu, B.; Azizzadenesheli, K.; Bhattacharya, K.; Stuart, A.; Anandkumar, A. Neural Operator: Learning Maps Between Function Spaces With Applications to PDEs. *Journal of Machine Learning Research* **2023**, *24*, 1–97.
- (37) Brandstetter, J.; van den Berg, R.; Welling, M.; Gupta, J. K. Clifford Neural Layers for PDE Modeling. International Conference on Learning Representations. 2023.
- (38) Li, Z.; Kovachki, N.; Azizzadenesheli, K.; Liu, B.; Bhattacharya, K.; Stuart, A.; Anandkumar, A. Neural operator: Graph kernel network for partial differential equations. *arXiv preprint arXiv:2003.03485* **2020**,
- (39) Brandstetter, J.; Welling, M.; Worrall, D. E. Lie Point Symmetry Data Augmentation for Neural PDE Solvers. Proceedings of the 39th International Conference on Machine Learning. 2022; pp 2241–2256.
- (40) Jin, P.; Meng, S.; Lu, L. MIONet: Learning multiple-input operators via tensor product. *SIAM Journal on Scientific Computing* **2022**, *44*, A3490–A3514.

- (41) Gupta, G.; Xiao, X.; Bogdan, P. Multiwavelet-based Operator Learning for Differential Equations. *Advances in Neural Information Processing Systems*. 2021.
- (42) Li, Z.; Meidani, K.; Farimani, A. B. Transformer for Partial Differential Equations' Operator Learning. *Transactions on Machine Learning Research* **2023**,
- (43) Hao, Z.; Wang, Z.; Su, H.; Ying, C.; Dong, Y.; Liu, S.; Cheng, Z.; Song, J.; Zhu, J. GNOT: A General Neural Operator Transformer for Operator Learning. *Proceedings of the 40th International Conference on Machine Learning*. 2023; pp 12556–12569.
- (44) Ovadia, O.; Kahana, A.; Stinis, P.; Turkel, E.; Karniadakis, G. E. ViTO: Vision Transformer-Operator. *arXiv preprint arXiv:2303.08891* **2023**,
- (45) Lu, L.; Meng, X.; Cai, S.; Mao, Z.; Goswami, S.; Zhang, Z.; Karniadakis, G. E. A comprehensive and fair comparison of two neural operators (with practical extensions) based on FAIR data. *Computer Methods in Applied Mechanics and Engineering* **2022**, *393*, 114778.
- (46) Bhattacharya, K.; Hosseini, B.; Kovachki, N. B.; Stuart, A. M. Model reduction and neural networks for parametric PDEs. *The SMAI journal of computational mathematics* **2021**, *7*, 121–157.
- (47) Chen, T.; Chen, H. Universal approximation to nonlinear operators by neural networks with arbitrary activation functions and its application to dynamical systems. *IEEE Transactions on Neural Networks* **1995**, *6*, 911–917.
- (48) Li, Z.; Kovachki, N.; Azizzadenesheli, K.; Liu, B.; Bhattacharya, K.; Stuart, A.; Anandkumar, A. Neural Operator: Graph Kernel Network for Partial Differential Equations. **2020**,
- (49) Wen, G.; Li, Z.; Azizzadenesheli, K.; Anandkumar, A.; Benson, S. M. U-FNO—An

- enhanced Fourier neural operator-based deep-learning model for multiphase flow. *Advances in Water Resources* **2022**, *163*, 104180.
- (50) Tran, A.; Mathews, A.; Xie, L.; Ong, C. S. Factorized Fourier Neural Operators. The Eleventh International Conference on Learning Representations. 2023.
 - (51) Guibas, J.; Mardani, M.; Li, Z.; Tao, A.; Anandkumar, A.; Catanzaro, B. Efficient Token Mixing for Transformers via Adaptive Fourier Neural Operators. International Conference on Learning Representations. 2022.
 - (52) Boullé, N.; Kim, S.; Shi, T.; Townsend, A. Learning Green’s functions associated with time-dependent partial differential equations. *Journal of Machine Learning Research* **2022**, *23*, 1–34.
 - (53) Tang, J.; Azevedo, V. C.; Cordonnier, G.; Solenthaler, B. Neural Green’s function for Laplacian systems. *Computers & Graphics* **2022**, *107*, 186–196.
 - (54) Li, Z.; Zheng, H.; Kovachki, N.; Jin, D.; Chen, H.; Liu, B.; Azizzadenesheli, K.; Anandkumar, A. Physics-Informed Neural Operator for Learning Partial Differential Equations. **2023**,
 - (55) Wang, S.; Wang, H.; Perdikaris, P. Learning the solution operator of parametric partial differential equations with physics-informed DeepONets. *Science Advances* **2021**, *7*, eabi8605.
 - (56) Lorsung, C.; Farimani, A. B. PICL: Physics Informed Contrastive Learning for Partial Differential Equations. 2024.
 - (57) Lorsung, C.; Li, Z.; Farimani, A. B. Physics Informed Token Transformer for Solving Partial Differential Equations. 2024.
 - (58) Razavi, A.; Van den Oord, A.; Vinyals, O. Generating diverse high-fidelity images with vq-vae-2. Advances in neural information processing systems. 2019.

- (59) Esser, P.; Rombach, R.; Ommer, B. Taming transformers for high-resolution image synthesis. Proceedings of the IEEE/CVF conference on computer vision and pattern recognition. 2021; pp 12873–12883.
- (60) Rombach, R.; Blattmann, A.; Lorenz, D.; Esser, P.; Ommer, B. High-resolution image synthesis with latent diffusion models. Proceedings of the IEEE/CVF conference on computer vision and pattern recognition. 2022; pp 10684–10695.
- (61) Zeng, X.; Vahdat, A.; Williams, F.; Gojcic, Z.; Litany, O.; Fidler, S.; Kreis, K. LION: Latent Point Diffusion Models for 3D Shape Generation. Advances in Neural Information Processing Systems. 2022.
- (62) Stachenfeld, K.; Fielding, D. B.; Kochkov, D.; Cranmer, M.; Pfaff, T.; Godwin, J.; Cui, C.; Ho, S.; Battaglia, P.; Sanchez-Gonzalez, A. Learned Simulators for Turbulence. International Conference on Learning Representations. 2022.
- (63) Pant, P.; Doshi, R.; Bahl, P.; Barati Farimani, A. Deep learning for reduced order modelling and efficient temporal evolution of fluid simulations. *Physics of Fluids* **2021**, *33*, 107101.
- (64) Hsieh, J.-T.; Zhao, S.; Eismann, S.; Mirabella, L.; Ermon, S. Learning Neural PDE Solvers with Convergence Guarantees. International Conference on Learning Representations. 2019.
- (65) Fresca, S.; Manzoni, A. POD-DL-ROM: Enhancing deep learning-based reduced order models for nonlinear parametrized PDEs by proper orthogonal decomposition. *Computer Methods in Applied Mechanics and Engineering* **2022**, *388*, 114181.
- (66) Lee, K.; Carlberg, K. T. Deep Conservation: A Latent-Dynamics Model for Exact Satisfaction of Physical Conservation Laws. 2021; pp 277–285.

- (67) Wiewel, S.; Becher, M.; Thürey, N. Latent Space Physics: Towards Learning the Temporal Evolution of Fluid Flow. *Computer Graphics Forum* **2019**, *38*.
- (68) Vlachas, P. R.; Arampatzis, G.; Uhler, C.; Koumoutsakos, P. Multiscale simulations of complex systems by learning their effective dynamics. *Nature Machine Intelligence* **2022**, *4*, 359–366.
- (69) Wang, T.; Wang, C. Latent Neural Operator for Solving Forward and Inverse PDE Problems. *arXiv preprint arXiv:2406.03923* **2024**,
- (70) Kontolati, K.; Goswami, S.; Em Karniadakis, G.; Shields, M. D. Learning nonlinear operators in latent spaces for real-time predictions of complex dynamics in physical systems. *Nature Communications* **2024**, *15*, 5101.
- (71) Morton, J.; Jameson, A.; Kochenderfer, M. J.; Witherden, F. Deep Dynamical Modeling and Control of Unsteady Fluid Flows. *Advances in Neural Information Processing Systems*. 2018.
- (72) Li, Y.; He, H.; Wu, J.; Katabi, D.; Torralba, A. Learning Compositional Koopman Operators for Model-Based Control. *International Conference on Learning Representations*. 2020.
- (73) Lusch, B.; Kutz, J. N.; Brunton, S. L. Deep learning for universal linear embeddings of nonlinear dynamics. *Nature Communications* **2018**, *9*, 4950.
- (74) Takeishi, N.; Kawahara, Y.; Yairi, T. Learning Koopman Invariant Subspaces for Dynamic Mode Decomposition. *Advances in Neural Information Processing Systems*. 2017.
- (75) Pan, S.; Duraisamy, K. Physics-Informed Probabilistic Learning of Linear Embeddings of Nonlinear Dynamics with Guaranteed Stability. *SIAM Journal on Applied Dynamical Systems* **2020**, *19*, 480–509.

- (76) Fresca, S.; Dede', L.; Manzoni, A. A comprehensive deep learning-based approach to reduced order modeling of nonlinear time-dependent parametrized PDEs. *Journal of Scientific Computing* **2021**, *87*, 1–36.
- (77) Hemmasian, A.; Barati Farimani, A. Reduced-order modeling of fluid flows with transformers. *Physics of Fluids* **2023**, *35*.
- (78) Hemmasian, A.; Farimani, A. B. Multi-scale Time-stepping of Partial Differential Equations with Transformers. 2023.
- (79) Patil, S.; Li, Z.; Barati Farimani, A. Hyena neural operator for partial differential equations. *APL Machine Learning* **2023**, *1*, 046114.
- (80) Yin, Y.; Kirchmeyer, M.; Franceschi, J.-Y.; Rakotomamonjy, A.; patrick gallinari Continuous PDE Dynamics Forecasting with Implicit Neural Representations. The Eleventh International Conference on Learning Representations. 2023.
- (81) Rojas, C. J.; Dengel, A.; Ribeiro, M. D. Reduced-order model for fluid flows via neural ordinary differential equations. *arXiv preprint arXiv:2102.02248* **2021**,
- (82) Chen, R. T. Q.; Rubanova, Y.; Bettencourt, J.; Duvenaud, D. K. Neural Ordinary Differential Equations. Advances in Neural Information Processing Systems. 2018.
- (83) van den Oord, A.; Vinyals, O.; kavukcuoglu, k. Neural Discrete Representation Learning. Advances in Neural Information Processing Systems. 2017.
- (84) Vaswani, A.; Shazeer, N.; Parmar, N.; Uszkoreit, J.; Jones, L.; Gomez, A. N.; Kaiser, L. u.; Polosukhin, I. Attention is All you Need. Advances in Neural Information Processing Systems. 2017.
- (85) Zhang, H.; Goodfellow, I.; Metaxas, D.; Odena, A. Self-Attention Generative Adversarial Networks. Proceedings of the 36th International Conference on Machine Learning. 2019; pp 7354–7363.

- (86) Guo, R.; Cao, S.; Chen, L. Transformer Meets Boundary Value Inverse Problems. International Conference on Learning Representations. 2023.
- (87) Li, Z.; Shu, D.; Farimani, A. B. Scalable Transformer for PDE Surrogate Modeling. Thirty-seventh Conference on Neural Information Processing Systems. 2023.
- (88) He, K.; Zhang, X.; Ren, S.; Sun, J. Deep Residual Learning for Image Recognition. Proceedings of the IEEE Conference on Computer Vision and Pattern Recognition (CVPR). 2016.
- (89) Ulyanov, D.; Vedaldi, A.; Lempitsky, V. Instance normalization: The missing ingredient for fast stylization. *arXiv preprint arXiv:1607.08022* **2016**,
- (90) Ba, J. L.; Kiros, J. R.; Hinton, G. E. Layer normalization. *arXiv preprint arXiv:1607.06450* **2016**,
- (91) Trockman, A.; Kolter, J. Z. Patches Are All You Need? *Transactions on Machine Learning Research* **2023**, Featured Certification.
- (92) Tolstikhin, I.; Houlsby, N.; Kolesnikov, A.; Beyer, L.; Zhai, X.; Unterthiner, T.; Yung, J.; Steiner, A. P.; Keysers, D.; Uszkoreit, J.; Lucic, M.; Dosovitskiy, A. MLP-Mixer: An all-MLP Architecture for Vision. Advances in Neural Information Processing Systems. 2021.
- (93) Nichol, A. Q.; Dhariwal, P. Improved Denoising Diffusion Probabilistic Models. Proceedings of the 38th International Conference on Machine Learning. 2021; pp 8162–8171.
- (94) Reynolds, O. IV. On the dynamical theory of incompressible viscous fluids and the determination of the criterion. *Philosophical transactions of the royal society of london.(a.)* **1895**, 123–164.
- (95) Launder, B. E.; Spalding, D. B. The numerical computation of turbulent flows. **1983**, 96–116.

- (96) Rognebakke, O. F.; Faltinsen, O. M. Sloshing induced impact with air cavity in rectangular tank with a high filling ratio. 20th international workshop on water waves and floating bodies. 2005; pp 217–20.
- (97) Faltinsen, O. M.; Rognebakke, O. F.; Lukovsky, I. A.; Timokha, A. N. Multidimensional modal analysis of nonlinear sloshing in a rectangular tank with finite water depth. *Journal of fluid mechanics* **2000**, *407*, 201–234.
- (98) Vahdat, A.; Kreis, K.; Kautz, J. Score-based Generative Modeling in Latent Space. Advances in Neural Information Processing Systems. 2021.
- (99) Hendrycks, D.; Gimpel, K. Gaussian error linear units (gelus). *arXiv preprint arXiv:1606.08415* **2016**,
- (100) Wu, Y.; He, K. Group normalization. Proceedings of the European conference on computer vision (ECCV). 2018; pp 3–19.
- (101) Issa, R. I. Solution of the implicitly discretised fluid flow equations by operator-splitting. *Journal of computational physics* **1986**, *62*, 40–65.
- (102) Patankar, S. V. Numerical methods in heat transfer. International Heat Transfer Conference Digital Library. 1982.

Supporting Information Available

6 Details for model implementation

In this section we provide the detail for the model architecture and hyperparameter choice of different models considered in this paper.

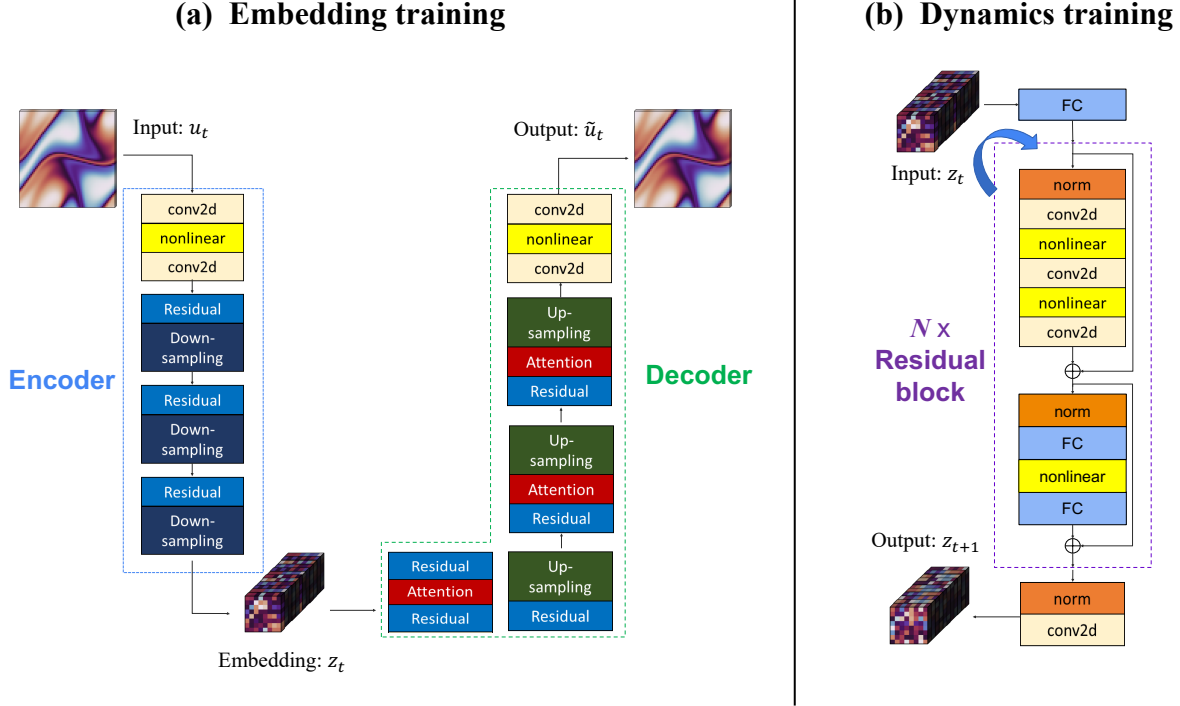


Figure 8: Detail architecture of the convolution based autoencoder and dynamics propagator. ”**conv2d**”: a convolution layer with 3×3 kernel, stride 1 and padding 1; ”**nonlinear**”: a non-linear activation function (we use Gaussian Error Linear Units (GELU)⁹⁹ throughout different experiments); ”**FC**”: a fully-connected layer which applies learnable linear transformation to the input; ”**Attention**”: self-attention layer defined in (5); ”**norm**”: normalization layer, where we use group normalization¹⁰⁰ throughout different experiments.

The residual block is defined as a stack of convolutional layers and non-linear activation function with skip connection: $a^{(l+1)} = \text{conv2d} \circ \text{nonlinear} \circ \text{conv2d}(a^{(l)}) + a^{(l)}$. For the downsampling layer, it is a convolution layer with 3×3 kernel and a stride of 2, no padding. This downsamples the mesh resolution by 2 along each axis. For the upsampling, it is a composition of nearest interpolation and a convolution layer with 3×3 kernel, stride 1 and padding 1.

Table 5: Hyperparameters for architectures used for 2D Navier-Stokes. For convolution layers that involve padding, we use circular padding in all directions. For the specification of UNet and Autoencoder, the width indicates the number of feature channels at different resolutions (the first one corresponds to the input grid and the last one corresponds to the latent grid), and Attn (attention) indicates if any attention mechanism is used at the specific resolution. # res. blocks indicates how many residual blocks are used at each resolution.

(a) FNO Hyperparameters		(b) UNet Hyperparameters	
Parameter	Setting	Parameter	Setting
Modes	16	Width	(64, 64, 128, 128)
Width	64	Attn	(false, false, false, true)
# Blocks	4	# res. blocks	2
Init lr	5e-4	Init lr	5e-4
Lr schedule	Cosine AnNeal	Lr schedule	Cosine AnNeal
Training Epochs	500	Training Epochs	500
Batch size	32	Batch size	32
(c) (Latent) Resnet Hyperparameters		(d) Autoencoder Hyperparameters	
Parameter	1D/2D	Parameter	Setting
Width	128	Width	(64, 64, 128, 128)
Dilation	2	Attn	(false, false, false, true)
# blocks	3	# res. blocks	2
Init lr	5e-4	Latent resolution	8×8
Lr schedule	Cosine AnNeal	Latent channel	16
Training Epochs	500	Init lr	3e-5
Batch size	32	Lr schedule	Constant
		Training Epochs	500
		Batch size	32

Table 6: Hyperparameters for architectures used for 2D Shallow-water equation. For convolution layers that involve padding, we use circular padding in x-direction and constant padding (zero) in y-direction.

(a) FNO Hyperparameters		(b) UNet Hyperparameters	
Parameter	Setting	Parameter	Setting
Modes (y/x)	32/16	Width	(64, 64, 128, 128)
Width	64	Attn	(false, false, false, true)
# blocks	4	# res. blocks	2
Init lr	5e-4	Init lr	5e-4
Lr schedule	Cosine Aneal	Lr schedule	Cosine Aneal
Training Epochs	500	Training Epochs	500
Batch size	32	Batch size	32
(c) (Latent) Resnet Hyperparameters		(d) Autoencoder Hyperparameters	
Parameter	Setting	Parameter	Setting
Width	128	Width	(64, 64, 128, 128)
Dilation	3	Attn	(false, false, false, true)
# blocks	4	# res. blocks	2
Init lr	5e-4	Latent resolution	12×24
Lr schedule	Cosine Aneal	Latent channel	64
Training Epochs	500	Init lr	3e-5
Batch size	32	Lr schedule	Constant
		Training Epochs	500
		Batch size	32

Table 7: Hyperparameters for architectures used for Tank sloshing problem. For convolution layers that involve padding, we use constant padding. When using longer training rollout horizon in FNO, we decrease the batch size to reduce computational cost.

(a) FNO Hyperparameters		(b) UNet Hyperparameters	
Parameter	Setting	Parameter	Setting
Modes (y/x)	32/16	Width	(64, 64, 128, 128)
Width	64	Attn	(false, false, false, true)
# blocks	4	# res. blocks	2
Init lr	5e-4	Latent resolution	7×15
Lr schedule	Cosine Anneal	Latent channel	64
Training Epochs	100 (80)	Init lr	5e-4
Batch size	32 (16)	Lr schedule	Cosine Anneal
		Training Epochs	100
		Batch size	32
(c) (Latent) Resnet Hyperparameters		(d) Autoencoder Hyperparameters	
Parameter	Setting	Parameter	Setting
Width	128	Width	(64, 64, 128, 128)
Dilation	3	Attn	(false, false, false, true)
# blocks	4	# res. blocks	2
Init lr	5e-4	Latent resolution	7×15
Lr schedule	Cosine Anneal	Latent channel	64
Training Epochs	100	Init lr	3e-5
Batch size	32	Lr schedule	Constant
		Training Epochs	100
		Batch size	32

7 Details for tank sloshing data generation

The equations that define the two equation $k - \epsilon$ model are reproduced below:

$$\begin{aligned}\frac{D(\rho k)}{Dt} &= \frac{\partial}{\partial x_j} \left[\left(\mu + \frac{\mu_t}{\sigma_k} \right) \frac{\partial k}{\partial x_j} \right] + \mu_t \left(\frac{\partial \bar{u}_i}{\partial x_j} \frac{\partial \bar{u}_i}{\partial x_j} + \frac{\partial \bar{u}_j}{\partial x_i} \frac{\partial \bar{u}_i}{\partial x_j} \right) - \rho \epsilon, \\ \frac{D(\rho \epsilon)}{Dt} &= \frac{\partial}{\partial x_j} \left[\left(\mu + \frac{\mu_t}{\sigma_\epsilon} \right) \frac{\partial \epsilon}{\partial x_j} \right] + C_1 \frac{\epsilon}{k} \mu_t \left(\frac{\partial \bar{u}_i}{\partial x_j} \frac{\partial \bar{u}_i}{\partial x_j} + \frac{\partial \bar{u}_j}{\partial x_i} \frac{\partial \bar{u}_i}{\partial x_j} \right) - C_2 \frac{\rho \epsilon^2}{k}\end{aligned}\tag{20}$$

where σ_k and σ_ϵ are the Prandtl numbers relating the diffusion of turbulent kinetic energy k and the rate of turbulent kinetic energy dissipation ϵ to the turbulent viscosity μ_t ($\sigma_k = 1.0$, $\sigma_\epsilon = 1.3$). C_1 , C_2 are empirical constants ($C_1 = 1.44$, $C_2 = 1.92$). The turbulent viscosity is defined based on k , ϵ , and the constant C_μ as

$$\mu_t = \rho C_\mu \frac{k^2}{\epsilon}\tag{21}$$

where $C_\mu = 0.09$.

The tank sloshing simulation is solved using the Pressure Implicit Splitting of Operators (PISO) scheme, which decomposes the solution operators into implicit prediction and explicit correction steps¹⁰¹. The PRESTO (Pressure Staggering) pressure correction scheme is used to interpolate between the cell-defined pressure values to determine the pressure defined at the mesh faces, which is necessary for the momentum update equations¹⁰².

The simulation is conducted using a uniform grid mesh, where the size of each element is $\Delta x = 0.01$ m, for a total of 7200 grid cells. A uniform timestep of $\Delta t = 0.005$ s is used with a first-order implicit timestepping scheme. A sensitivity study was performed to identify a suitable spatio-temporal discretization able to resolve the dynamics of the process (Figure 9). The transient variation of the gauge pressure at a reference point $x = 0.6$ m, $y = 0.36$ m within the domain is examined as a metric for simulation mesh-independence, for mesh elements $0.25\times$, $0.5\times$, $2\times$, and $4\times$ the size of the original mesh grid size. A similar study is used to identify a suitable time discretization, with the transient gauge pressure examined at $0.25\times$, $4\times$ and $8\times$ the reference Δt used for simulation.

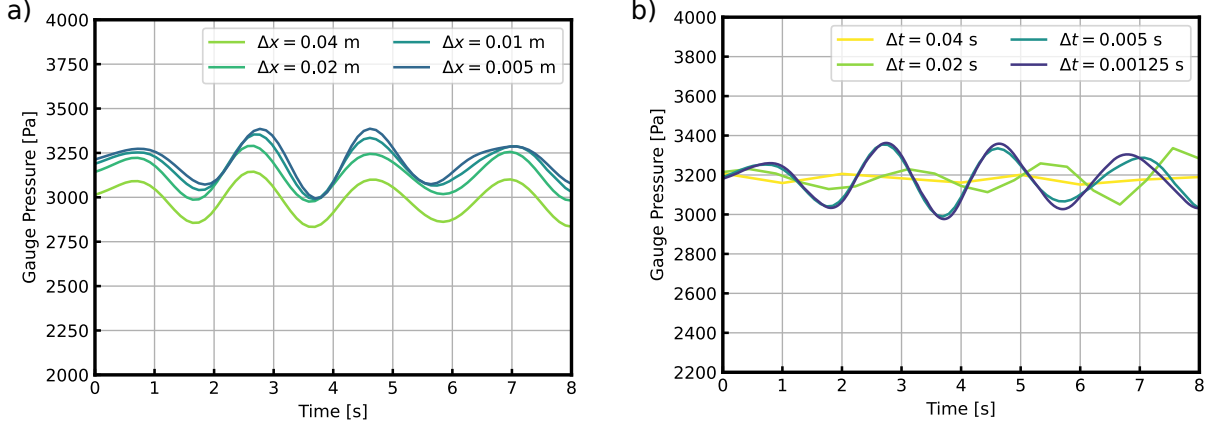


Figure 9: (a) A mesh convergence study on the tank sloshing simulation. The gauge pressure is taken at the reference point $x = 0.6$ m, $y = 0.36$ m, and the time increment is $\Delta t = 0.005$ s. The spatial discretization used in this work is $\Delta x = 0.01$ m. (b) A time discretization convergence study on the tank sloshing simulation. The gauge pressure is taken at the reference point $x = 0.6$ m, $y = 0.36$ m. The spatial discretization is held constant at $\Delta x = 0.01$ m, and the time increment of $\Delta t = 0.005$ s is used in this work.

8 Ablation on encoder/decoder training

In this section we present a study on the influence of different training strategies of the encoder/decoder ($\phi(\cdot), \psi(\cdot)$) and the propagator network ($\gamma(\cdot)$). The first strategy is to train the propagator network and encoder/decoder separately as we have introduced in the main text, which we will refer to as "Two stage" training in the below discussion. The training of the encoder/decoder can also be combined with the propagator, where the networks' parameters are optimized by minimizing the combination of reconstruction loss and dynamics prediction loss (the training rollout steps is m):

$$L = \frac{1}{L} \sum_{m=1}^{m=L} \|u_{t+m} - \psi(\underbrace{\gamma \circ \gamma \circ \dots \circ \gamma}_{\times m}(\phi(u_t)))\|_2^2. \quad (22)$$

In addition, we can combine the encoder/decoder with the propagator network together $\gamma_{\text{combined}} = \psi \circ \gamma \circ \phi$, which is equivalent to a UNet without any skip connections but only

a bottleneck. We denote the model trained on the combined loss as "Combined loss" and the model formed by combining three sub-networks as "Combined architecture". Lastly, we study another popular encoding scheme where the discretization will not be altered during encoding/decoding process - the encode-process-decode (EPD) scheme^{4,5,7}. More specifically, we compared against the Dilated CNN with MLP-based encoder/decoder used in Stachenfeld et al.⁷.

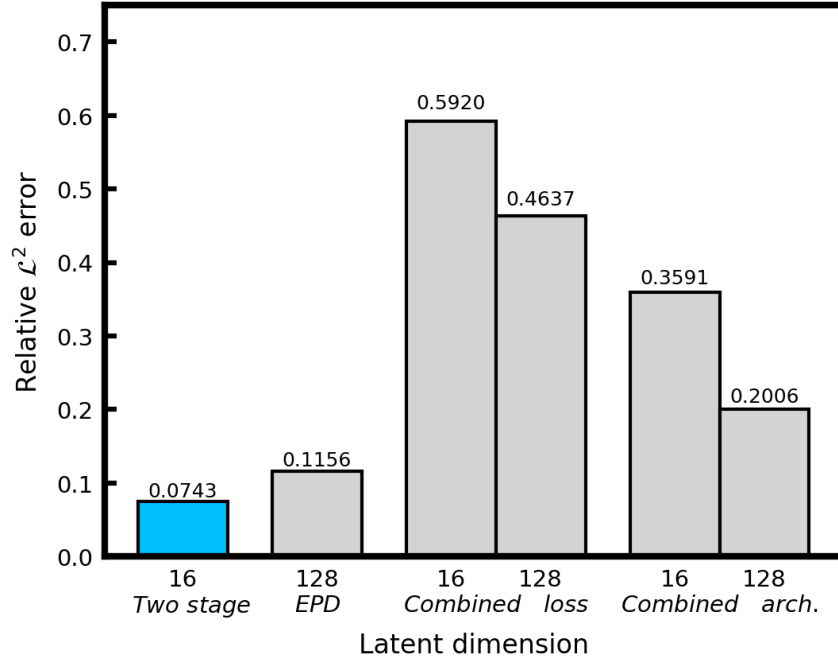


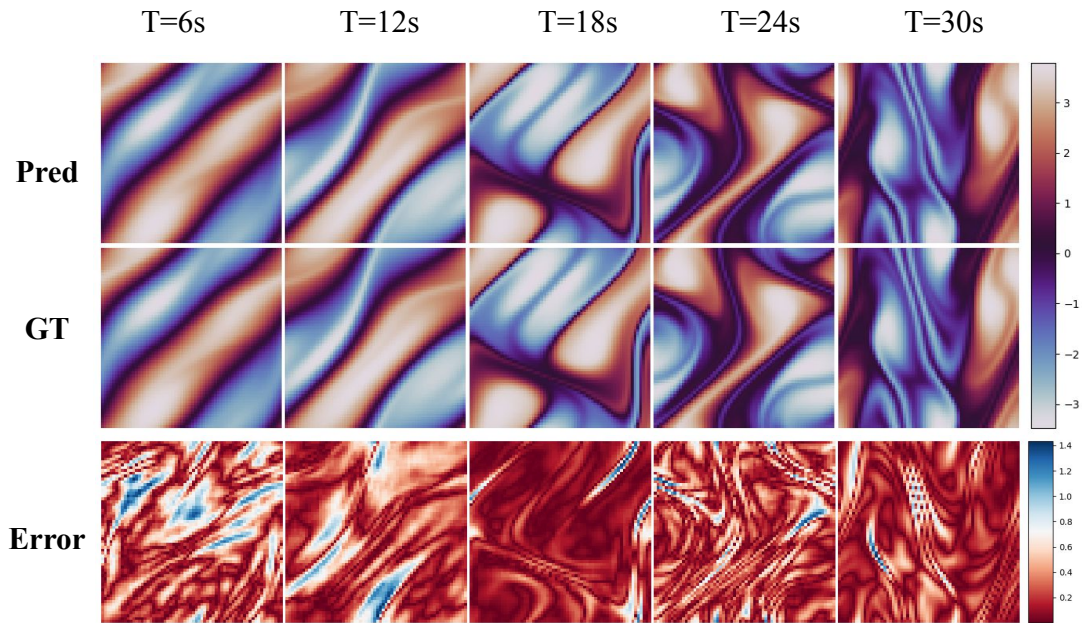
Figure 10: Rollout error of different models on 2D Navier-Stokes equation.

As shown in Figure 10, training encoder/decoder jointly with propagator results in a degraded performance especially if the dimension of the bottleneck are chosen to be relatively small. With a larger latent dimension, the jointly trained model still cannot match the performance of a model that employs two stage training. We hypothesize the degradation of the performance of joint training is due to the difficulty of optimization. When jointly training the autoencoder and the propagator, the encoder is being updated at every optimization step and thus the latent dynamics for propagator to approximate is always changing along the course of training. This poses an optimization challenge for the propagator network. On the

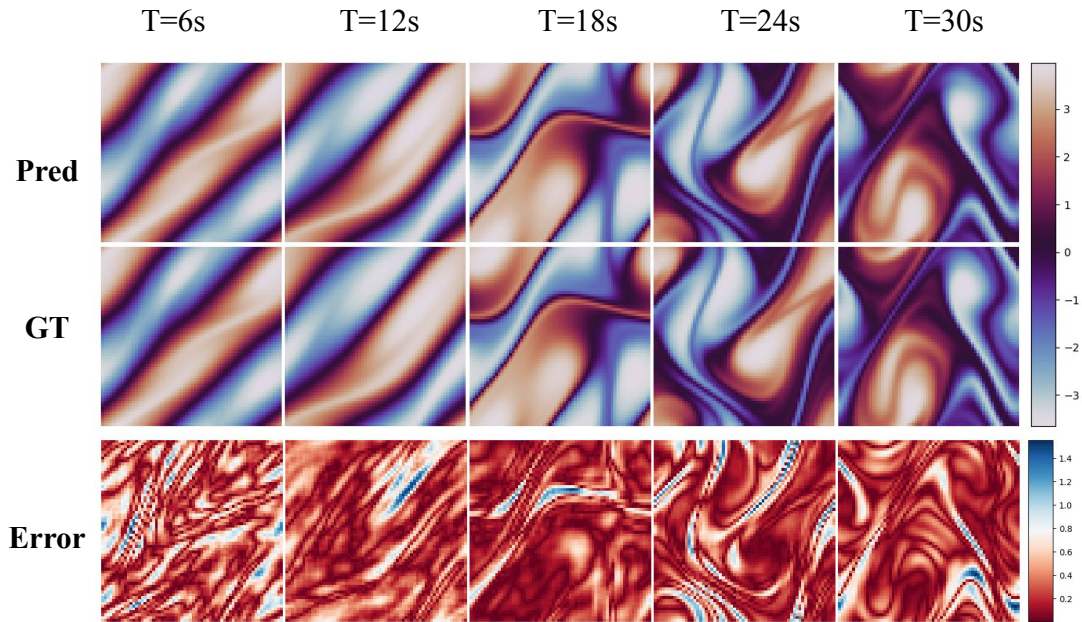
other hand, the encoder/decoder need to balance between learning an embedding space that’s easier for propagator to predict the forward dynamics and an embedding space that can achieve minimum reconstruction error. When training the autoencoder and dynamics propagator separately, the training objective is de-coupled so it eases the difficulty of the optimization process without the need to balance the reconstruction and dynamics propagation loss with a carefully selected loss weight. For the combined architecture variant, it under-performs two stage model and also the UNet benchmarked in the main manuscript. Compared to UNet, it does not have multi-scale skip connection. This increases the difficulty for the optimization as mesh reduction at each level will lose some high-frequency information, while in UNet the skip-connection at different scales can preserve these high-frequency features. It is worth noting that in two stage training the encoder/decoder also does not have skip connection to preserve the high-frequency features on the higher resolution grid, but it is trained to learn to reconstruct them in the first stage training. We postulate that reconstructing high-frequency components is easier than predicting high-frequency components of the future frames, which results in a combined architecture model variant performs worse and requires much more latent channels to reach reasonable accuracy. Furthermore, our proposed model is able to outperform the encode-process-decode scheme on this NS2D problem despite the dynamics propagator operates on a very coarse latent field.

9 Visualization

9.1 Navier-Stokes 2D

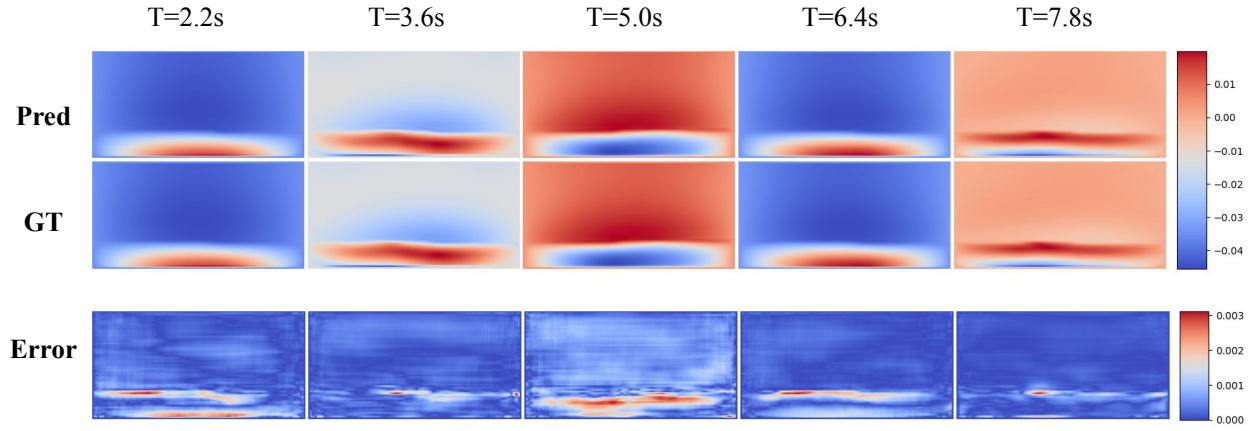


(a) Sample prediction 1 of the vorticity field.

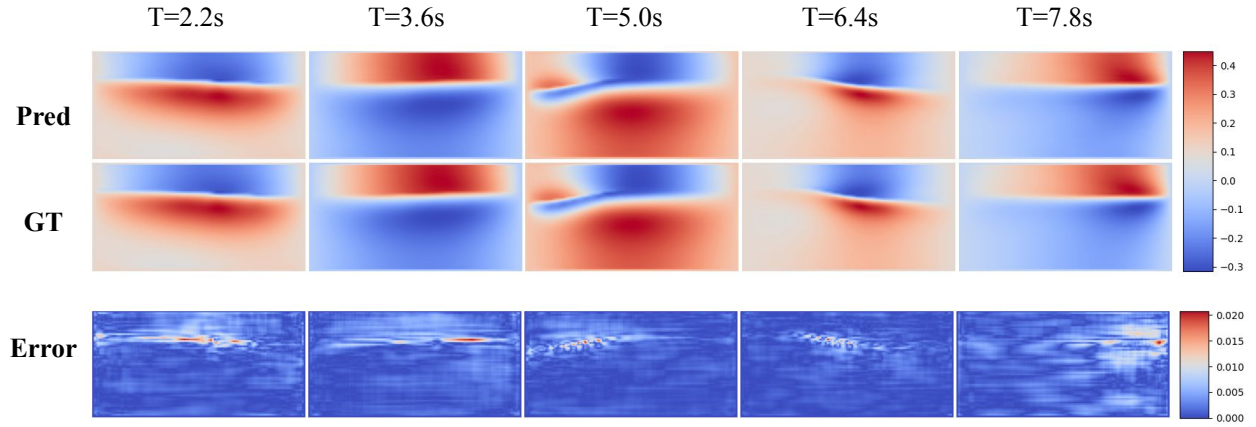


(b) Sample prediction 2 of the vorticity field.

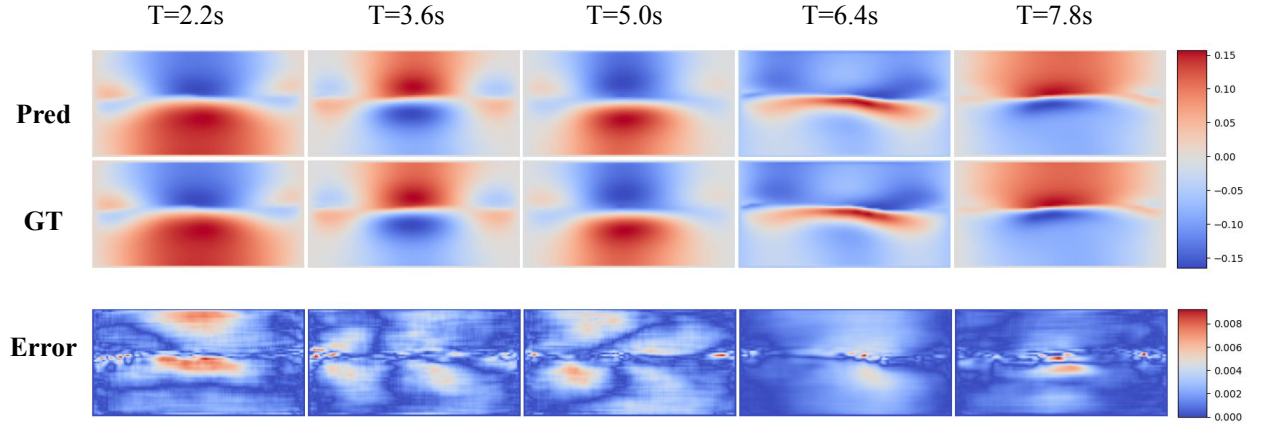
9.2 Tank sloshing



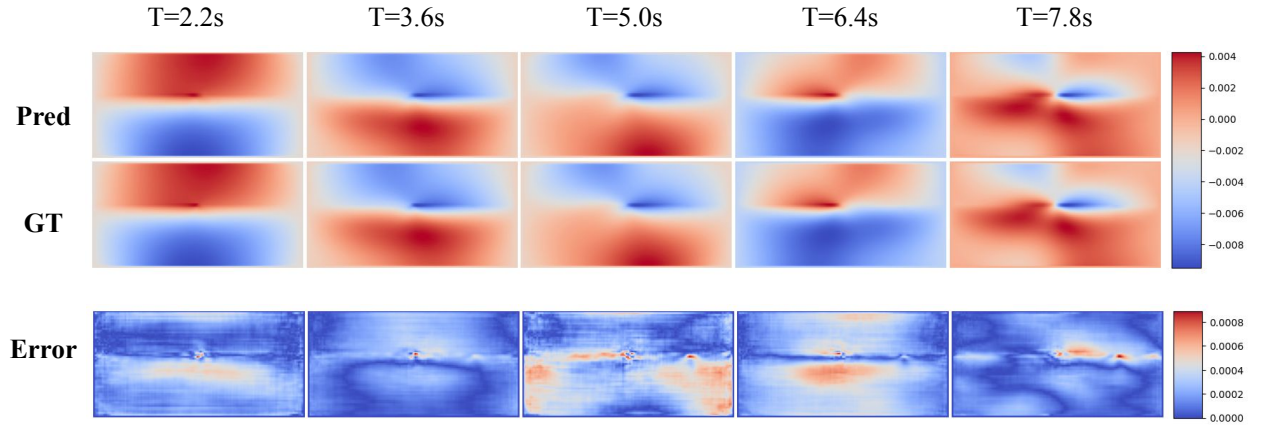
(a) Sample prediction 1 of the x -component of the velocity field \mathbf{u} with liquid surface height: $h = 15$. Unit: m/s .



(b) Sample prediction 2 of the x -component of the velocity field \mathbf{u} with liquid surface height: $h = 44$. Unit: m/s .

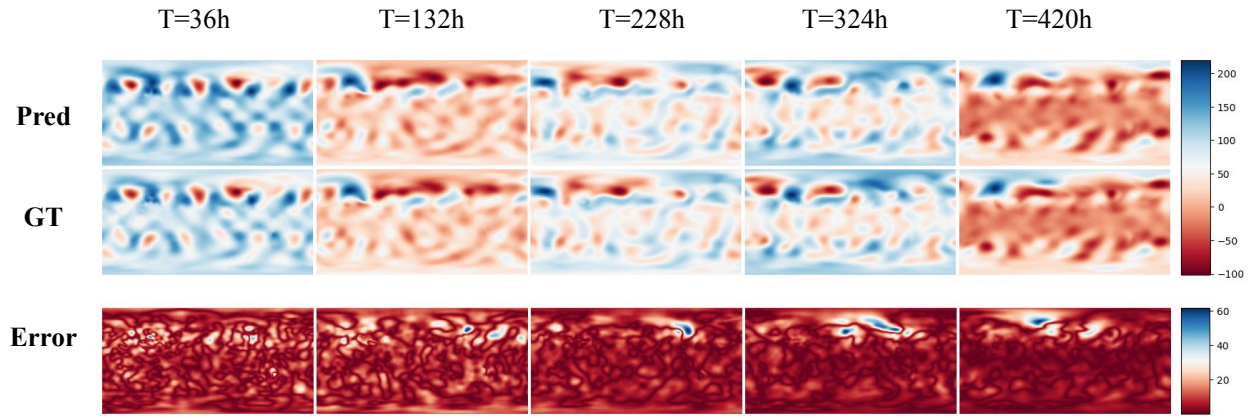


(a) Sample prediction 1 of the x -component of the velocity field \mathbf{u} with oscillation frequency: $\omega = 7.12$ rad/s. Unit: m/s .

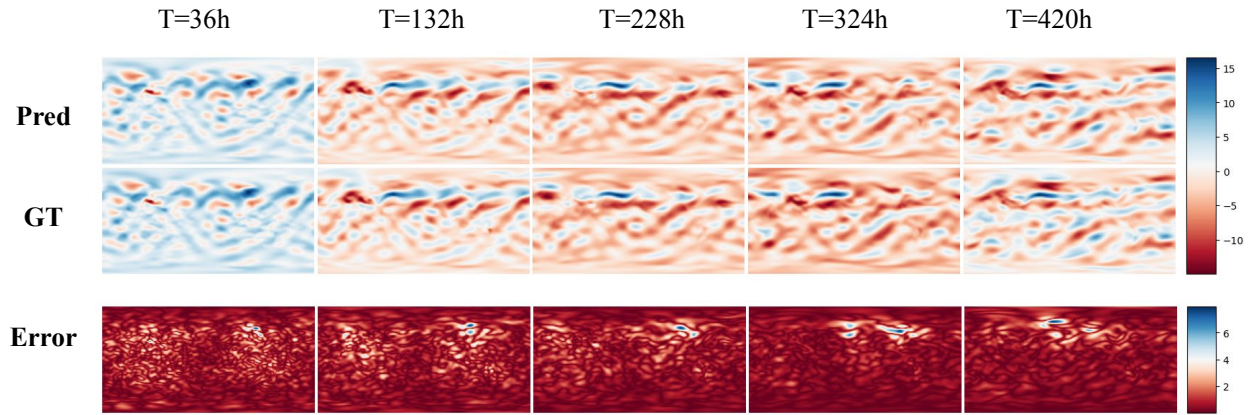


(b) Sample prediction 2 of the x -component of the velocity field \mathbf{u} with oscillation frequency: $\omega = 1.47$ rad/s. Unit: m/s .

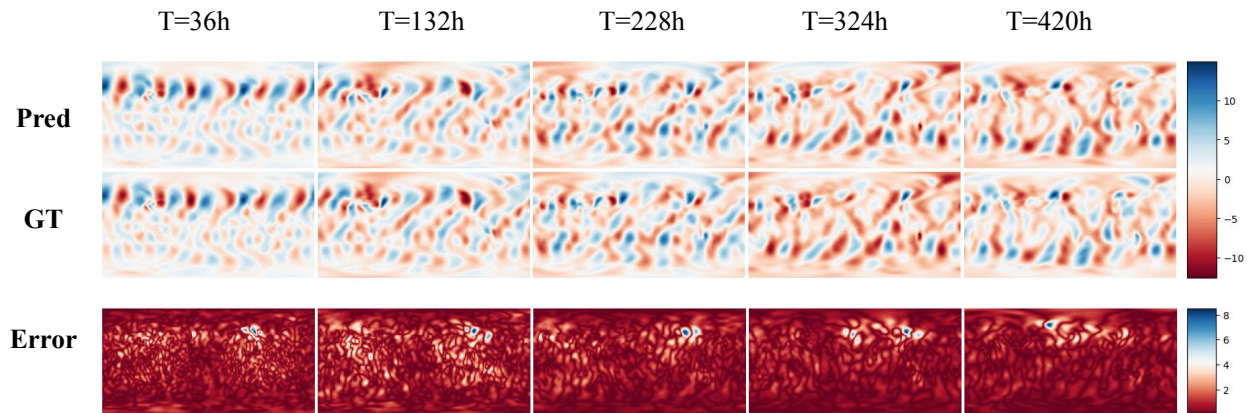
9.3 Shallow water



(a) Sample prediction of pressure field η . Unit: Pa .



(b) Sample prediction of the x -component of velocity field u_x . Unit: m/s .



(c) Sample prediction of the y -component of velocity field u_y . Unit: m/s .